On Path Length, Beam Divergence, and

Retroreflector Size in Open Path FTIR Spectroscopy

by

Cameron Power

A Thesis Submitted to
Saint Mary's University, Halifax, Nova Scotia
in Partial Fulfillment of the Requirements for the Degree of
Bachelor of Science with Honours in Astrophysics

April, 2021, Halifax, Nova Scotia

© Cameron Power, 2021

Approved:

Approved:

Date: July 30, 2021

Abstract

On Path Length, Beam Divergence, and Retroreflector Size

in Open Path FTIR Spectroscopy

By Cameron Power

Open-Path Fourier Transform InfraRed (OP-FTIR) spectroscopy is an established technique used to measure boundary layer trace gas concentrations, consisting of a spectrometer and a retroreflector separated by a measurement path. The detection limit is directly proportional to the optical path, which controls target gas spectral absorption feature depth; however, depending on the specifics of the spectrometer and telescope optics, beam divergence can begin overfilling the distant retroreflector array for paths greater than ~300 m, resulting in decreased returning radiation. In this case, the absorption signature of the target gas increases, but the signal to noise ratio of the recorded spectrum does not, making detection difficult. The results of an experiment where the retroreflector array area was increased to collect a larger fraction of returning radiation at path lengths ranging from ~200 m − 1000 m are discussed, including an analysis of both underlying spectra and quality indicators for retrieved concentrations of carbon monoxide. The results show that the larger retroreflector array results in smaller decreases in the signal-to-noise ratio as a function of the measurement path when compared to a smaller array. Next, the effectiveness of cleaning retroreflector arrays after extended field use is presented using quantitative information, including 1) a measured 10% increase in infrared intensity and 3) surface characterization of a single retroreflector cube corner array

before and after the cleaning process, which resulted in no notable changes, but revealed corrosive processes and contaminants present on the cube. Lastly, the results of theoretical spectral simulations are discussed in detail for CO and HCHO (formaldehyde) showing how path length, water concentration, and target concentration affect the differential absorption spectrum of the target, also considering random and systematic noise levels. It was determined that path lengths > 300 m are necessary for robust HCHO measurements. A further 10 common atmospheric species are explored in Appendix B. Finally, spectral simulations also explore the relationship between absorbance and transmittance by increasing the target gas concentration, from which it is seen that for less abundant trace gases (i.e., HCHO at 1 ppb) concentration and transmittance are approximately linearly related.

Date: July 30, 2021

Acknowledgements

Contents

List of Figures

Glossary of Terms

- HITRAN - High-Resolution Transmission Molecular Spectroscopic Database

- IR - InfraRed

- MALT - Multiple Atmospheric Layer Transmission Radiative Transfer Code

- NLLS - Non-Linear Least Squares fitting algorithm

- OP-FTIR - Open-Path Fourier Transform InfraRed Spectroscopy

- RH - Relative Humidity

- SEM - Scanning Electron Microscope

- RMS - Root Mean Square

Chapter 1

Introduction and Motivation

1.1 Air Pollution and Climate Change

One of the most socially relevant fields of scientific research today is that of air quality and climate change processes. This is due to the increasingly large human impact on Earth's atmosphere, which has raised concerns around air quality and long term effects on the planet. Climate change research is important due to the necessity to both quantify and understand the changes occurring, along with the need for evidence of these changes and attribution to human causes to a broader audience.

Green house gases lead to climate change, which is a long term effect while the issue of air pollution adversely affects entire populations on shorter scales. In particular, a critical component to both climate change and air quality are trace gases. Trace gases appear in very small

concentrations, and only constitute a fraction of the atmosphere (~1%) while causing longterm health risks if one experiences prolonged exposure of high concentrations. For example, carbon dioxide, methane, and nitrogen dioxide, three important trace gases when discussing green house gases, have background levels of 400 ppm, 1.8 ppm, and 320 ppb respectively (IPCC, 2013). One of the more versatile and novel methods of measuring these trace gases is Open-Path Fourier Transform Infrared (OP-FTIR) spectroscopy, discussed next.

1.2 Overview of the OP-FTIR

OP-FTIR spectroscopy is an established technique used to measure boundary layer trace gas concentrations, e.g., in "fenceline monitoring" of industrial emissions. The measurement is made by sending an infrared beam to a distant retroreflector and recording the returned signal spectrum, which contains signatures of multiple trace gas absorptions in the beam path. This results in a path-averaged measurement, which means that measurements are representative of a selected path, as opposed to a point, while retaining high precision. This is an inherent advantage to the open-path system, as it provides a more

representative look at the measurement location, and minimizes the effect of localized emissions.

The OP-FTIR system consists of a spectrometer, which contains an infrared source, telescope, mirror optics, a retroreflector separated by a measurement path as seen in Figure 1.1, and detectors. The source in the spectrometer generates infrared light which is collimated by the telescope into a 30 cm beam toward the retroreflector, this beam passes through the atmosphere along the measurement path until it reaches the retroreflector, where the beam is then reflected back to the spectrometer to be recaptured. The measurement path is typically a few hundred meters, at which distance returning signal diminishes significantly, thus greatly degrading measurements.
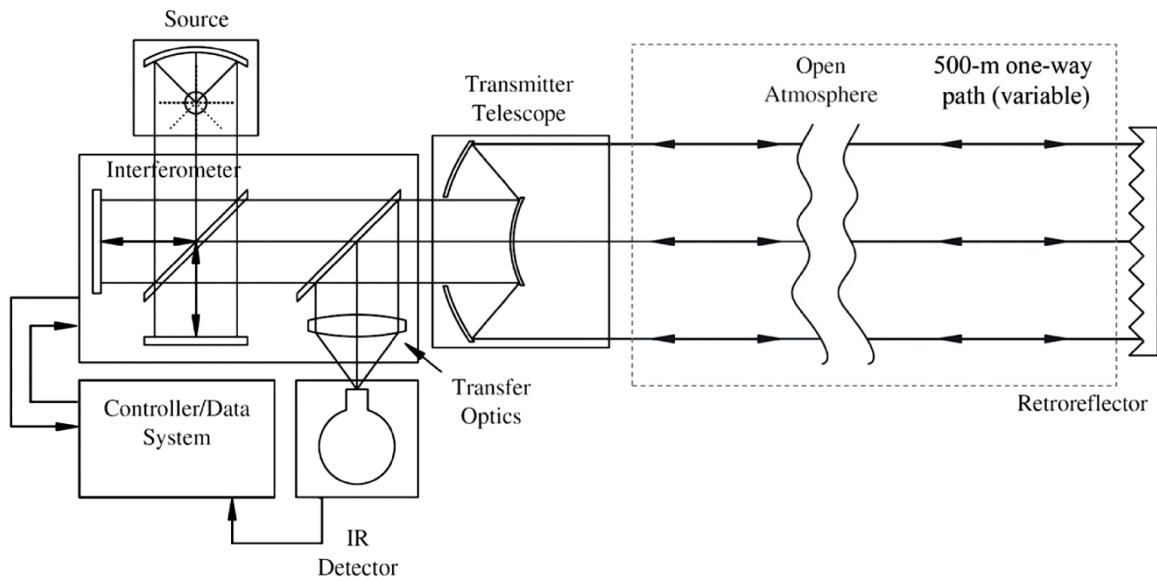
Figure 1.1: OP-FTIR schematic (adapted from Jarvis, 2003).

The result of these measurements is an atmospheric absorption spectrum which can be used to determine trace gas concentrations by analyzing the features of the spectrum (see section 1.5).

1.2.1   Contrasting OP-FTIR and *In Situ*

When considering methods for trace gas observations, the OP-FTIR spectroscopy system and *in situ gas* analyzers are among the most popular choices. Although these methodologies differ quite significantly in their spatial sampling of trace gases, they have been used in tandem to provide comparisons and references, such as the study conducted by Griffith et al. (2017) where open-path measurements were compared to *in situ* measurements at one end of the path. When comparing the two methods to one another, both have inherent strengths and weaknesses. In the case of OP-FTIR spectroscopy, measurements are representative of a selected path, as opposed to a point, while retaining high precision; however, according to Smith et al. (2011), this is to the detriment of accuracy (Smith et al., 2011) due to calibration difficulties in the open path. By comparison, calibrated *in situ* measurements are by definition

very accurate, and, according to Griffith "Such point-based in situ measurements in clean baseline air are well suited to monitoring long term global changes in atmospheric greenhouse gases..." (Griffith, 2017, p. 1549). However, *in situ* point measurements are, by definition, only representative of a single point, and not of an extended atmospheric path. Thus, for an urban setting such as Halifax, open-path systems are less sensitive to highly localized emissions, thus allowing for a more accurate representation of the deployment area (e.g. Waxman et al., 2017). Compared to *in situ* point measurement systems, OP-FTIR spectroscopy is relatively novel, with ongoing developments, and improvements to techniques and configurations, such as the size of the retroreflector used. This is one of the primary motivations for this research project: quantifying the effect of a larger retroreflector on the results of the OP-FTIR system.

1.3 Retroreflector Array Design and Size

Retroreflector arrays are constructed from multiple cube corner retroreflectors, which can have various coatings depending on the

wavelength of light the system utilizes. In the case of infrared light, the most commonly used coatings are gold and silver, due to their high reflectivity in the infrared regime (Bennett, 1965). Each cube corner retroreflector reflects any incoming light back toward the source in a slightly translated path (~6 cm), parallel to the incoming path (Figure 1.2 (right)). This is accomplished by combining three flat mirrors so that each is perpendicular to one another (Figure 1.2 (left)). This results in any incoming beam being reflected twice to achieve a direction change of 180°, i.e., a retro-reflection.
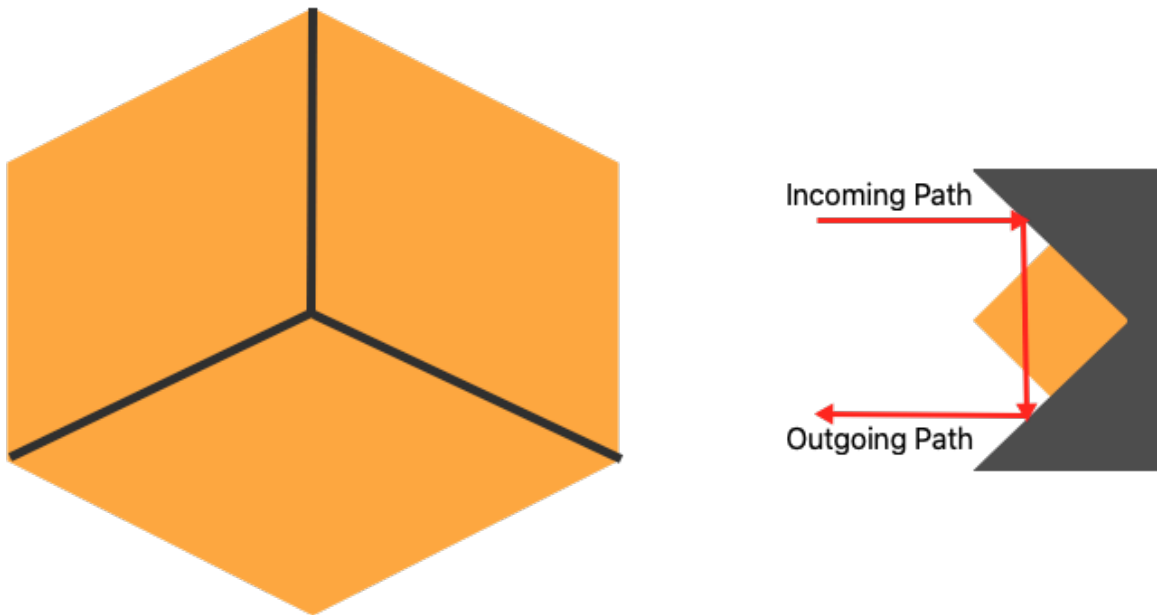
Figure 1.2: Cube corner retroreflector seen from front (left). Cube corner retroreflector seen from side with example incoming beam double reflection (right).

1.3.1   Beam Divergence and Overfilling

An important variable in OP-FTIR spectroscopy is the optical path length, as it directly correlates to the detection limit of the system (a longer path implies lower detection limits). At long path lengths, however, beam divergence due to imperfect beam collimation causes a decrease in returning long-path radiation due to overfilling of the retroreflector array (Figure 1.3). In this simplified schematic of a mono-static arrangement, the source (not shown), spectrometer (not shown) and telescope (cylinder) are on the left, while the retroreflector array (two pieces) is on the right. The bi-directional red arrows show the IR radiation travelling along the open path. A larger array, or a composite array, has the ability to return more divergent radiation towards the source and the co-located detector.
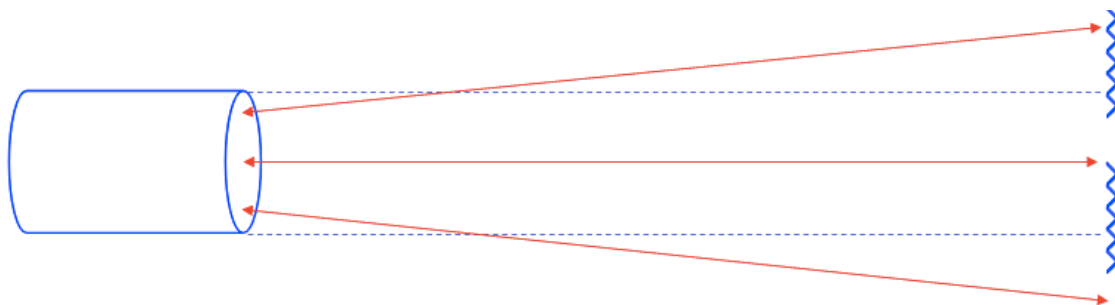
Figure 1.3: Beam divergence (greatly exaggerated) in long-path OP-FTIR spectroscopy (Power, 2020 American Geophysical Union).

As a result, this increases the threshold path at which the returning signal is too greatly diminished due to of beam divergence, thus increasing the maximum path length at which the OP-FTIR system can make reliable measurements.

1.4 Absorption Spectra

An absorption spectrum is a measure of radiation absorption at a given wavelength; in the case of infrared spectroscopy, this absorption is a result of the rotational and vibrational transitions of molecular compounds (Bacsik, 2004). Based on these unique absorption signatures, infrared spectroscopy can be used to quantitatively analyze a spectrum for underlying trace gas concentrations.

1.4.1 Spectral Fitting

Fitting an absorption spectrum involves matching a measured spectrum to a simulated spectrum. The simulated spectrum includes a list of i gases, comprised of the target gas, which is the gas that is being studied, and the interfering gases, which includes all other gases in the

spectral region, apart from the target gas. This region is defined in terms of spatial frequency, wavenumber, and is dictated by the characteristics of the compound's infrared transitions from reference literature, i.e., HITRAN.

In the spectral fit, each gas contains k rotational-vibrational absorption features, which are calculated using line-by-line constants from the HITRAN database. The rotational-vibrational absorption features are the result of transitions in rational and vibrational energy states (Griffith, 2002), which are the result of rotation about the centre of mass of a molecule and the stretching of the bonds between atoms in a molecule respectively. These transitions are discrete, quantized energy levels, which leads to each compound absorbing at specific wavelengths (Banwell & MacCash, 1994).

As an indication of the quality of the fit, the root-mean-square residual can be calculated between the fitted and measured spectrum, where large root-mean-square residual values indicate poorer fit quality.

1.4.2 Calculating Transmittance

To calculate the absorbance at a given wavenumber, ν, first, the ith gas absorption coefficient, α_i, needs to be determined using the following,

$$\alpha_i(\nu) = \sum_k S_{i,k}(T, \nu - \nu_0) \otimes V(P, T, \nu) \, ,$$

where k is the absorption line in a rational-vibrational band at a central wavenumber ν_o, S is line strength, P is pressure, T is temperature and V is the Voigt line shape (Wiacek and Strong, 2008, and references there in).

The spectral line shape is a description of the form of the kth absorption feature. The line shape can take three ideal forms, Gaussian, Lorentzian, and Voigt, where the Voight function is a convolution of the Gaussian and Lorentzian functions. These functions are described by the following,

$$\text{Gaussian:} \quad f(\bar{\nu} - \bar{\nu}_0) = \frac{1}{\sqrt{\pi}\gamma_D} exp\left(- \frac{(\bar{\nu} - \bar{\nu}_0)^2}{\gamma_D^2} \right) \, ,$$

$$\text{Lorentz:} \quad f(\bar{\nu} - \bar{\nu}_0) = \frac{1}{\pi} \frac{\gamma_L}{(\bar{\nu} - \bar{\nu}_0)^2 + \gamma_L^2} \; ,$$

$$\text{Voigt} = \text{Lorentz} \otimes \text{Gaussian} \; ,$$

where γ_L is the Lorenz broadening coefficient, and γ_D is the Doppler broadening coefficient. Transition line broadening is dictated primarily by Lorentz broadening in the lower atmosphere (high pressure), while in the upper atmosphere (high velocity), transition line broadening is dictated primarily by Doppler broadening. This results in the Lorenz contribution dominating in the OP-FTIR technique, due to the relatively high pressure of operation (1 atm) (Griffith, 1996).

Through summing over all gases, i, the optical depth can be calculated using the absorption coefficient as,

$$\tau(\nu) = \sum_i a_i \alpha_i(\nu) \; ,$$

where a_i is the concentration of the ith gas multiplied by the measurement path length. This relates to the transmittance, T, through the following relation, using Beer's law,

$$T(\nu) = \frac{I(\bar{\nu})}{I_0(\bar{\nu})} = e^{-\tau},$$

where $I_0(\bar{\nu})$ is the intensity at a given wavenumber before passing through a given path, and $I(\bar{\nu})$ is the intensity after passing through a given path. Lastly, the transmittance relates to the absorbance, A, as (Bacsik, 2004),

$$T = 10^{-A}.$$

This relationship is shown graphically in Figure 1.4, which shows absorbance ranging from 10^{-5} to 10^{5} on the logarithmic x-axis, and transmittance on the y-axis ranging from 0 to 1. This figure shows the nonlinear relationship between absorbance and transmittance, which means an increase in absorbance by some factor does not result in an increase in transmittance by the same factor.
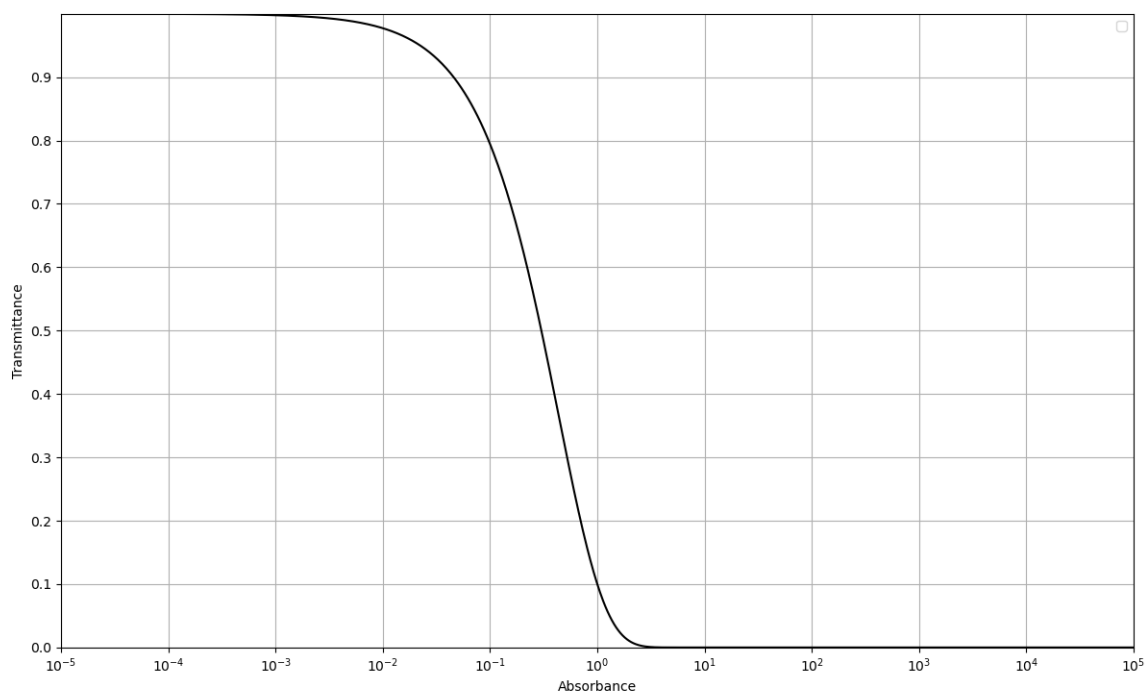
Figure 1.4: Logarithmic relationship between absorbance vs transmittance.

1.4.3 MALT Forward Model

A substantial portion of this project entails theoretical spectral simulations using the Multiple Atmospheric Layer Transmission (MALT) forward model (Griffith, 1996). This model utilizes spectral absorption parameters from the High-Resolution Transmission Molecular Spectroscopic (HITRAN) database (Gordon et al., 2017) to provide the non-linear mapping between trace gas concentrations and atmospheric absorption spectra. A non-linear least squares (NLLS)

algorithm is used to fit simulated spectra to measured spectra. To utilize

MALT, additional constraints in the form of input parameters are

required, which are, 1) initial concentrations of expected target and

interfering trace gases, 2) spectral continuum variables, 3) instrumental

parameters determined by the hardware configuration, and 4)

environmental variables of pressure and temperature which influence

the HITRAN parameters. The measured spectra are then fitted using

the Levenberg-Marquardt iterative minimization algorithm, which finds

a set of fit parameters (including gas concentrations) that minimize the

cost function, χ^2, based on the difference between the measured and

calculated (simulated) transmittance spectrum, T:

$$\chi^2 = \frac{\sum_v (T_{measured}(\nu) - T_{calculated})^2}{\epsilon_v^2} \, .$$

The retrieval results are the gas concentrations, as well as any other

parameters (1-4 above), that give the best fit of $T_{calculated}$ to $T_{measured}$, as

judged by a minimum value of the spectral residual.

1.5 Experimental Goals

The first half of this project explores the effect of changes to the retroreflector array used in the OP-FTIR system. This is achieved through 1) cleaning visually degraded retroreflectors, and 2) increasing the retroreflector array area. The remaining half of this project explores how parameters such as path length, (interfering) water concentration, and target gas concentration affect the differential absorption signatures of the target gas.

Chapter 2

Experimental Methods

2.1 Retroreflector Cleaning

After extensive field use, especially in coastal settings, retroreflectors begin to show signs of visual degradation as well as a decrease in infrared (IR) reflectivity. To mitigate this degradation and subsequent IR response decrease , the array can be cleaned to improve performance, however, the broader community using optical mirrors in environmental applications is divided as to the best cleaning procedures and their effectiveness in improving IR signal returns.

For this experiment, a method of deionized water and methanol application was used to clean a retroreflector array constructed in 2015, with ~180 days of cumulative exposure in a coastal setting. Successive applications (~15) of deionized water were applied to each side of each

cube corner retroreflector, then a final application of methanol was applied.

2.1.1 Surface Characterization

Scanning Electron Microscope (SEM) measurements were performed by Dr. Hanley of Saint Mary's University, Department of Geology, to characterize the cube corner surface before and after cleaning procedures. The SEM performs measurements on a sample by focusing a beam of electrons through a column of lenses. This column is directed at the sample chamber, which is evacuated along with the column to produce a vacuum. These electrons then impact the surface of the sample, producing secondary electrons, characteristic x-rays, and backscattered electrons. These products are then collected by detectors to form an image for surface characterization. The depth of penetration on the sample surface is dependent on factors such as the sample density, and beam acceleration, however, the penetration depth is usually on the order ~2 microns.

To determine the result of the cleaning, a selection of visible images were also taken by Dr. Hanley before and after the cleaning

process to examine the condition of the optical surface. These images were taken to determine the extent of the remaining contamination on the optical surface, as well as the buckling of the gold mirror foil off of the base of the cube corner retroreflector. Before and after cleaning characterization was very similar in the visible and SEM analysis, therefore only the "before" results are shown in Chapter 3.

Additionally, Field Emission-SEM surface characterization was conducted on a portion of the optical surface (~4 mm square) that bordered the edge of the optical surface, chosen to explore the topography and composition. These methods include the study of backscattered electrons, secondary electrons, as well as the use of an energy dispersive spectrometer.

2.1.2 Spectral Effects of Cleaning

To quantify the effect of cleaning on the retroreflector, FTIR spectral measurements were made before and after the cleaning process, at St. Mary's University. For the measurement before and after cleaning, the OP-FTIR telescope (modified 12" Schmidt-Cassegrain) was focused on the retroreflector array using an iterative procedure of a z-

adjustment of the secondary mirror (in-out from primary mirror) followed by an x-y adjustment of the telescope tube (left-right, up-down), which was iterated at least once to maximize signal levels. Focusing the telescope is particularly important at long path lengths, where returning radiation is reduced due to beam divergence. The result of these measurements are absorption spectra, recorded at 0.5 cm^{-1} resolution with 240 co-added interferogram samples in 1 minute. A Norton-Beer (medium) apodization was applied before transforming the time-averaged interferogram. This same iterative focusing process was also used to make spectroscopic measurements with the enlarged array, following the same acquisition settings (Section 2.2.2, p. 24).

2.2 Increasing Retroreflector Area

When considering the deployment location for the OP-FTIR system, there are many competing factors that need to be considered, including, electrical/internet capacity, shelter, and, most importantly, atmospheric sampling. An important factor that is often hard to control is the path length resulting from a given measurement location and how it affects the trace gas. The selected path length must, however, take into

account the limitations imposed on path length by the measurement system, those being an effective maximum and minimum path length.

A minimum path length of around 10 m or more is required to make effective measurements of trace gases other than the highly abundant water and carbon dioxide (Griffith, 2002). Additionally, an upper limit exists due to signal loss resulting from overfilling the retroreflector, though this is dependent on retroreflector size and specific beam collimation (Wiacek et al., 2018a). Measurements at longer path lengths are further complicated due to growing interference from water and carbon dioxide in the atmosphere.

Through enlarging the retroreflector in the initial portion of this project, the path length at which the retroreflector is overfilled can be increased. This, along with improved beam collimation can increase the maximum achievable path length before overfilling begins to affect measurements.

2.2.1 Larger Retroreflector Array Construction

To construct a larger retroreflector array, 60 new cube corner retroreflectors were sourced and purchased leading to the honours work

in the summer of 2020. These cube corner retroreflectors were purchased after an exhaustive search of possible candidates. Factors such as cost, reflective coating material (gold, silver, or aluminum), construction time, and protective coatings were considered. In particular, the mirror material and the protective coating were researched in detail as they directly affect both the quality of the measurements as well as the longevity of the retroreflectors. After a suitable retroreflector candidate was selected, the 60 pristine cubes arrived at Saint Mary's University already mounted onto two custom array panels (30 new cubes on each panel), to which the older cubes were subsequently added in the course of this project.

In October 2020, two existing retroreflector arrays, each comprising 59 bare-gold cube corner retroreflectors, of 63 mm diameter sourced in 2015, were disassembled to construct the larger retroreflector arrays. The smaller retroreflector array is shown in Figure 2.1 (top), taken in 2015. The larger retroreflector array that was constructed using these 59 bare-gold cube corners, which have since degraded somewhat from ~180 days of cumulative field use, and 30 pristine (newly purchased) gold cube corner retroreflectors, which have

a protective dielectric coating with a very similar high IR reflectivity

(~98%), is shown in Figure 2.1 (bottom), taken just after construction.

This increase by 30 cube corner retroreflectors corresponds to an

approximate 50% increase in the retroreflector array area.
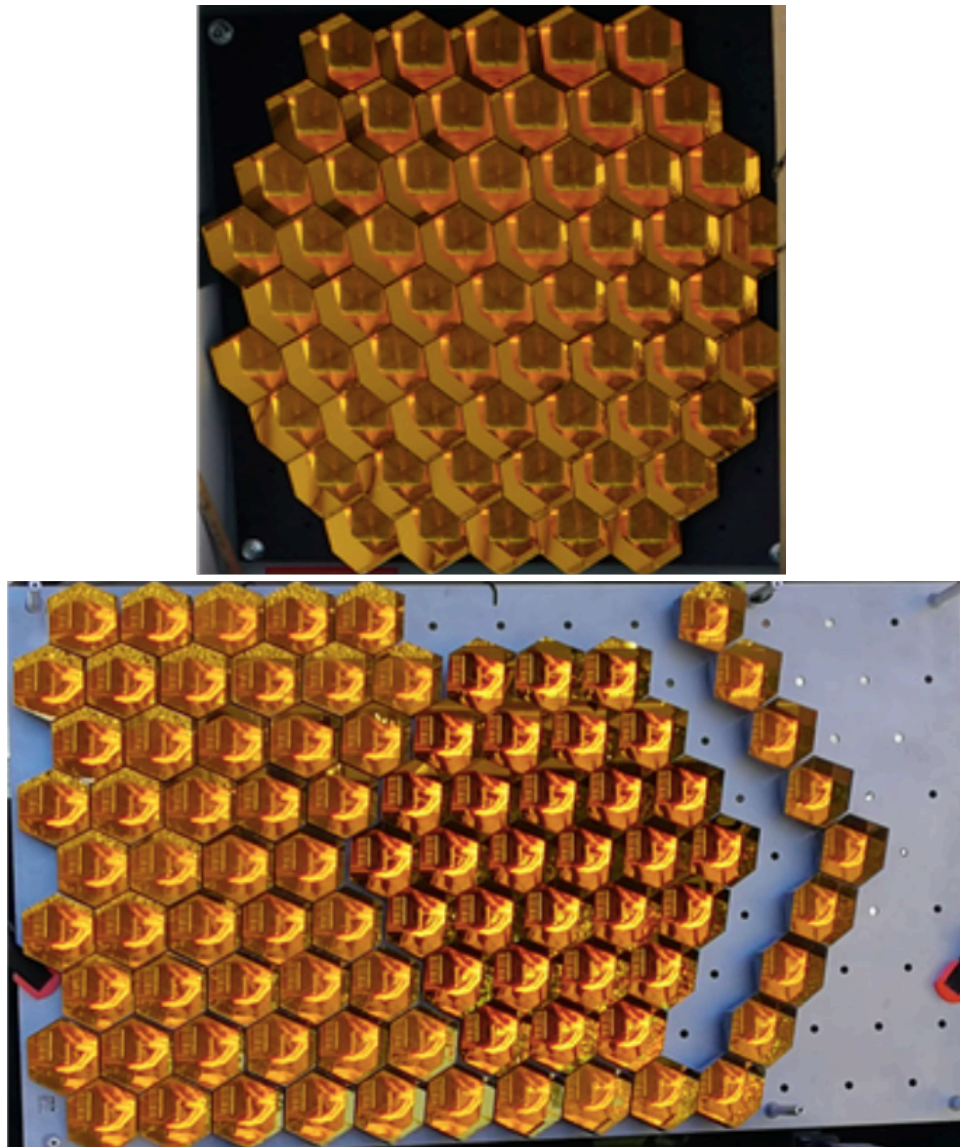

Figure 2.1: (Top) Pristine bare-gold retroreflector array acquired in 2015, (Bottom) Larger retroreflector array constructed in 2020, with the 30 pristine cube corner retroreflectors in the centre and somewhat degraded retroreflectors around it.

2.2.2 Varying Path Experiments

To determine the point at which beam divergence results in overfilling of a retroreflector for a particular system, an experiment can be conducted where spectral measurements are made at successively increasing path lengths. In May 2015, this style of experiment was conducted with a retroreflector array constructed of, at the time, 59 pristine bare-gold cube corner retroreflectors. The retroreflector array was progressively moved further from the spectrometer starting at 50 m and increasing to a separation of 450 m in 100 m increments. This resulted in two way separations of 100-900 m, where a two-way separation is double the physical separation between the retroreflector array and the spectrometer, representing the distance travelled by the beam. At each increment, spectroscopic measurements were made and the return signal level was recorded to assess beam divergence.

In October 2020, this experiment was repeated with the newly constructed retroreflector array. This experiment was conducted with separations from 50 m to 1575 m (two-way) in approximately 200 m increments, with the goal of assessing the benefits of the larger retroreflector array area, specifically with regard to overfilling. At each

location and path, the OP-FTIR telescope was focused on the retroreflector using the method outlined in section 2.1.2 (p. 19). Note that the data selected for analysis were those that were free of interference from local traffic while measurements were being made.

2.2.3   Spectroscopic Retrievals

After data acquisition using the proprietary software from Bruker (OPUS RS), the trace gas concentrations were retrieved using MALT. The raw and normalized spectra recorded at each path length of both the 2015 and 2020 experiments were plotted to assess gross features in the data. From the spectra normalized to the highest value, the region of $7640\ cm^{-1}$ to $7740\ cm^{-1}$ was isolated to determine the spectral noise by taking the standard deviation after de-trending. The de-trending removed any change in the mean signal of the region, thus making the signal in the region vary about zero so that a true random noise value could be calculated. The signal-to-noise ratio was calculated by taking the inverse of the noise value from these normalized spectra.

Retrievals of carbon monoxide were performed on the absorption spectra between 2044.52 cm⁻¹ and 2167.95 cm⁻¹ using a nonlinear least-

squares technique (Wiacek et al., 2018a) that models the absorption of all gases relevant in the chosen spectral window using the HITRAN database (Rothman et al., 2013) at the temperature and pressure of the measurements. The 2044.52 cm^{-1} and 2167.95 cm^{-1} region was selected as the best region to detect the target gas, carbon monoxide, with interfering gases of water and carbon dioxide, as both gases have notable absorbance in the selected region. To analyze the effect of path length (and thus noise), the root-mean-square residuals of the spectral fit and retrieved carbon monoxide concentration percent errors were chosen as goodness-of-fit parameters.

2.3 Theoretical Spectral Simulation

For each target trace gas with significant interfering gases present, there is an optimal path length to allow for sufficient spectral absorption for detection, before either the increasing path begins to yield diminishing returns due to an increase in the absorption of the interfering gases (Wiacek et al., 2018b) or retroreflector overfilling begins. Determining which trace gases have an optimal path length and also finding this optimal path length is the focus of the theoretical

spectral simulations in this project, which utilizes constant input parameters such as water concentration and target gas concentration while path length is varied to show its effect on absorption.

2.3.1 Effect of Path on Target Gas Absorption

To determine the effect of the path length on the absorption spectrum of the target and interfering gases, the path length must be allowed to vary over a range while all other parameters are held constant. These parameters include values for target gas concentration, any interfering gas concentrations, instrument parameters, temperature, and pressure.

Simulations were also conducted to isolate the effect of only the target gas on the spectrum. This is achieved by calculating the differential absorption due to the target gas, or in other words, the difference between a spectrum with the target and interfering gases, and a spectrum that contains only the interfering gases. These simulations require the same input parameters as above.

For the simulations in this project, multiple target gases were selected and simulated, however the focus for this project is carbon monoxide and formaldehyde due to their differing abundance, discussed further in the following section. The input parameters for these simulations, as well as the results outputs for various other trace gases, will be given in Appendices A and B.

2.3.2 Effect of Increasing Target Gas Concentration

To examine the relationship between transmittance and absorbance shown in Figure 1.4, simulations were conducted where the target gas concentration was increased by a factor of ten to examine the resulting effect on the differential absorption. These simulations were conducted for multiple gases, however the focus in the results section will be on carbon monoxide and formaldehyde. These gases were selected due to their differing background concentration values; carbon monoxide is abundant and easily detectable at ~120 ppb, while formaldehyde has a very low background concentration near the threshold of detection for the OP-FTIR system at ~1 ppb.

Chapter 3

Results and Discussion

3.1 Cleaning Experiments and Mirror Characterization

After ~15 campaigns spanning over 5 years of service, the smaller (59-cube) retroreflector arrays were cleaned to remove visual degradation and help mitigate a 15-25% IR signal intensity loss, determined experimentally in July of 2019. After recording spectral signals before and after the cleaning process, a maximum spectral intensity increase of ~10% was found. The visual degradation on the optical surface remained unchanged. An optical surface characterization of a single bare-gold cube corner mirror edge (Figure 3.1) was conducted by Dr. Hanley on one of the most degraded array elements, while an SEM (Figure 3.2) was used for a more detailed analysis. Before and after cleaning results proved very similar, hence

only before results are presented below. The following are Dr. Hanley's remarks on the characterization experiments, as presented by Power at the American Geophysical Union; Fall Meeting (2020).

There was virtually no change in imaging results after cleaning, including particles that remained affixed to the reflective area, which would require ultrasonic cleaning to remove, likely destroying the underlying gold coating in the process. Figure 3.1 shows that the base substrate holding the gold mirror coating is an aluminum-chromium alloy that is heavily surface oxidized/corroded, producing the aluminum-hydroxide visible principal contaminant. Figure 3.2 shows that the contaminants are only present in significant thickness on the outermost $500 \ \mu m$ of the surface, near the mirror edge, which corresponds to the area of visible contamination. As the aluminum-chromium alloy corrodes, gold is bubbled and separated from the substrate (Figure 3.1 inset), creating the visible area of damage ($500 \ \mu m$) up to several mm wide over all array cubes.

Shown in Figure 3.1 and inset, creep delamination is the de-adhesion of a coating from the substrate. As the retroreflectors see

continued use it is likely the effects of creep delamination will worsen, possibly resulting in peeling of the coating from the substrate.

Since these processes (gold buckling and heavy edge contamination by the Al phase) affect mirror optical flatness, the signal loss should be correlated with area lost, which we estimate (over all 3 mirrors of this heavily impacted cube) using a DIC Nomarski prism (Figure 3.1) to be no more than 3% of the total area (range between 1 and 3%). This is lower than the estimates of reflectivity loss of 15-25% over the entire array area. Additionally, the total reflectivity is approximately 100% in regions outside of the 500 um to 3 mm altered, buckled window, also measured in reflected, plane-polarized visible light, using a highly polished gold standard (0.2 um finish). However, the flatness and reflectivity characterizations are optical, whereas the 15-25% signal loss was inferred from mid-IR spectral intensity measurements in 2015 and again in 2019, although the complication of imaging an unknown fraction of degraded vs. pristine cubes makes a precise analysis impossible. Overall, the estimated signal loss is of the same order in each spectral region.
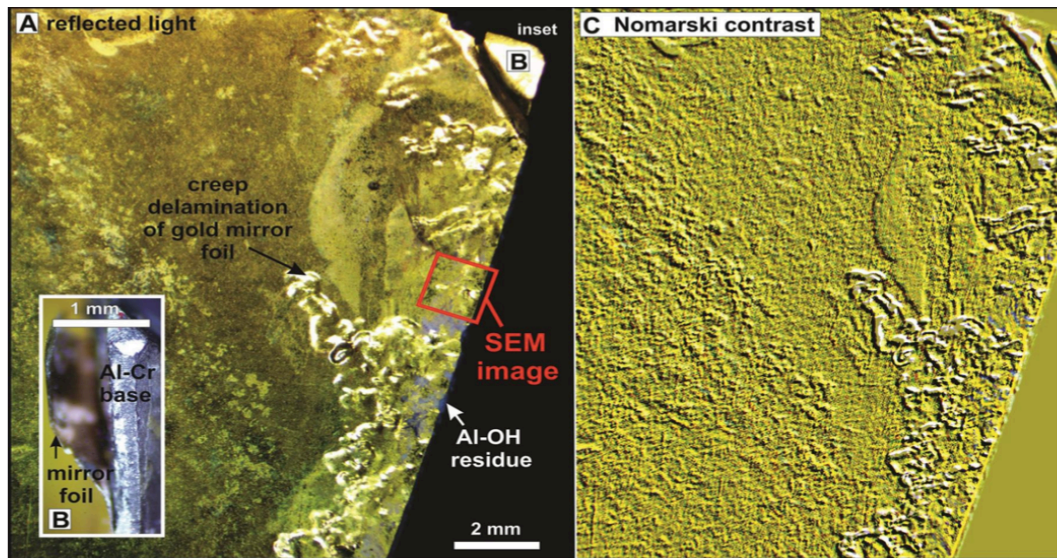
Figure 3.1. Visible image of single bare-gold cube corner edge before cleaning (left) and optical flatness characterization (right). "SEM image" refers to Figure 3.2 analysis area. Courtesy of Dr. Hanley
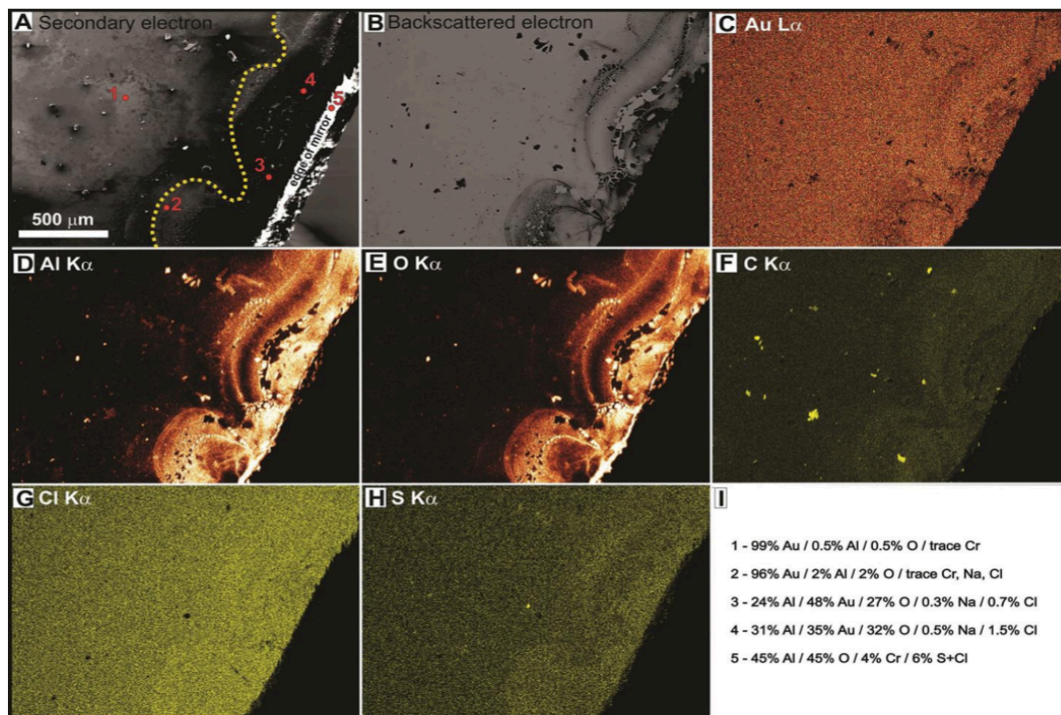

Figure 3.2. Field Emission-SEM surface characterization of a single bare-gold cube corner (before cleaning) showing compositional and textural features of a visibly contaminated mirror edge ("SEM image" in Figure 3.1) with back-scattered electron detector (BSE, panel A), secondary electron detector (SE, panel B), and energy dispersive spectrometer (EDS) analysis of points 1-5 (panel A) shown in panel I. See text for details about panels C-H. Courtesy of Dr. Hanley

In Figure 3.2, [A], the SE image shows surface textural features including a thin film of variable thickness (light and dark patches) and fragments of contaminating material that increases in abundance immediately near the edge of the mirror. The numbered spots were analyzed by EDS and data are summarized in Figure 3.2, [I]. The dashed yellow line outlines the area closest to the edge that is contaminated with a precipitate and delaminated. In Figure 3.2, [B], the BSE image shows grey scale mean atomic number (proportional to density). Black areas show pure, low density, coarse-grained contaminant particles on the mirror surface. Light areas are the gold surface coated with a variable density "film" of fine-grained contaminants in negligible concentrations. In Figure 3.2, [C]-[H], the EDS "maps" of relative X-ray line intensity (emission line used for measurement indicated next to element symbol). These maps show that the vast majority of the contaminants are concentrated within ~ 500 microns of the edge of the gold mirror. The dominant contaminant is an aluminum-bearing hydroxide (gibbsite- boehmite) seen in the aluminum and oxygen X-ray maps, Figure 3.2 [D, E] respectively, which is present in significant concentrations, up to ~ 50 wt% (mass

fraction) of the surface layer. Marine-related, minor to trace carbon (organics, coarse particles, and fine-grained film) in Figure 3.2, [F], chlorine (fine-grained film, likely halite – NaCl) in Figure 3.2, [G], and sulphur (fine-grained film) in Figure 3.2, [H] are also present in this ~500 micron zone. In panel [I] of Figure 3.2, there is a summary of EDS analysis at points 1-5 shown in Figure 3.2, [A], showing that generally, at least ~ 50% of the surface layer is gold, and away from the ~500 micron altered zoned, gold concentration rapidly climbs to ~99 wt%+, as expected for gold-coated cube corner retroreflectors without any protective dielectric coating.

3.2 Increasing Retroreflector Area

3.2.1 Effect on Raw Spectra

In the 2015 experiment at Franklyn Street (Figure 3.3), it was determined that after ~300 m of two-way separation between the spectrometer and retroreflector array, the retroreflector became overfilled and the signal intensity was progressively reduced at increasing paths, with an approximately even signal drop between 500 m and 700 m, and again between 700 m and 900 m (Figure 3.5). In the

2020 experiment at Otter Lake (Figure 3.4), the signal began decreasing to a similar extent after ~600 m of separation. The rate of decrease in 2020 was half the rate of the 2015 experiment, as shown by the slopes of best-fit lines in Figure 3.5. Apart from the expected slower signal decrease for a larger array, the arbitrary signal level maxima are 25% lower at Otter Lake (~0.69, 100 m) as compared to Franklyn Street (~0.92, 100 m), despite the 50% larger retro array, which is discussed in detail next. Note that when the arrays are under-filled, signal levels are expected similar, regardless of size.

Pressure and temperature, and the closely associated swings in humidity, are also factors in signal intensity. In the 2015 experiment, the conditions were slightly more humid than the conditions of the 2020 experiment, which would result in a decrease in the signal levels recorded in the 2015 experiment, as opposed to the observed increase. The higher humidity at Franklyn Street is also visible in the spectral features of water absorption (Figure 3.3 and 3.4, e.g., 100 m path in saturated band regions) and retrieved water concentrations (not shown).

The likelihood that the maximum signal level decreases in 2020 spectra were caused by the dielectric coating on the 30 pristine cubes

was also investigated. From the manufacturer's specifications, the reflectivity of the cube corner retroreflectors with the protective coating is similar or higher, i.e., 97-99%, as compared to bare-gold (97-98%). While Otter Lake spectra show a changed continuum shape between $800 \; cm^{-1}$ and $1200 \; cm^{-1}$ as compared to spectra recorded at Franklyn Street (Figure 3.3 compared to Figure 3.4), the recent mirror cleaning experiments involving uncoated gold cubes (not shown) have the simpler continuum shape of the spectra from Franklyn Street (Figure 3.3), but with similar maximum signal values of Otter Street. Thus it is confirmed that the signal decrease is not due to the protective dielectric coating, as expected.

The next potential source for the lower signal levels in the 2020 spectra that was investigated was the 59 degraded cube corner retroreflectors and how they affected the signal levels recorded at Otter Lake in 2020. It is not clear if the alignment procedure used (see section 2.1.2) has the precision or accuracy to image only the 59 degraded cube corner retroreflectors or some combination of old and new cubes. Since the array is under-filled at 100 m separation (12" telescope diameter), if the spectrometer was aligned with only degraded retroreflectors, their

measured degradation would account for the full observed signal loss of 25% (at 100 m path), assuming that nothing else has changed with the system since 2015. If the spectrometer was imaging a combination of degraded and pristine retroreflectors, it would imply that the degradation would have to be greater still (e.g., 50% if half of the imaged cubes were new, also assuming their reflectivity was 100%). This is not the case, however, as measurements from 2015 and 2019, which were made at similar conditions to one another, rule out a 50% degradation, even after ~180 cumulative days of ambient marine environment exposure since 2015, which contributes to the poor visible quality of the arrays.

Lastly, using the internal retroreflector in the spectrometer (used for calibration and computer connection), a measurement was taken at an extremely short path (< 1 m). This measurement revealed that the Globar infrared source intensity has decreased by ~10% between 2015 and 2020. A loss of source intensity would affect degraded and pristine cubes in the same way, so this factor can account for a significant portion of the 25% reduction in arbitrary signal levels (at 100 m) between 2015 and 2020, although the complication of imaging an

unknown fraction of degraded vs. pristine cubes makes a precise analysis impossible. Regardless of reduced absolute signal levels in 2020, the essential finding of this work stands: a larger retroreflector array exhibits slower signal loss as a function of separation from the
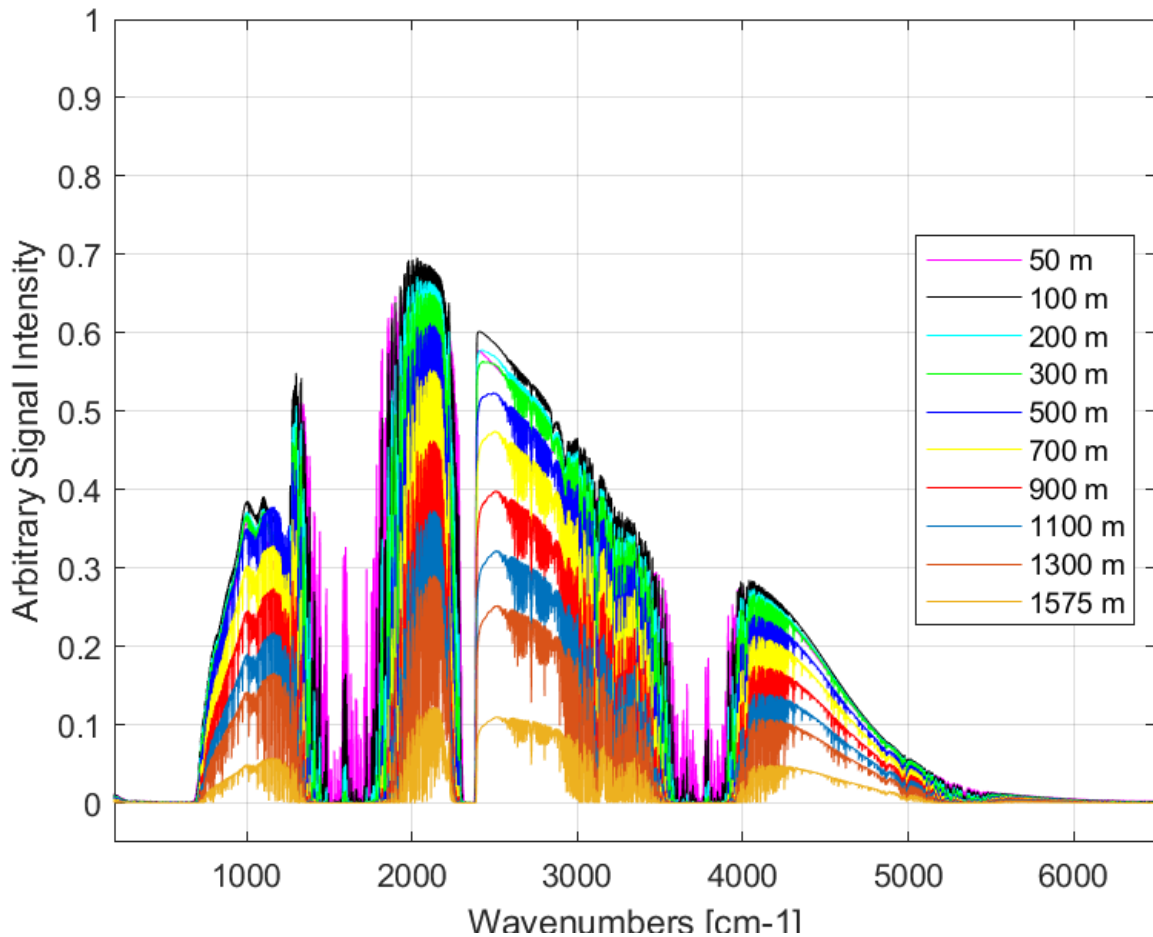

Figure 3.3. Raw spectra from Franklyn Street (May, 2015), where a 59-cube retroreflector array was used at varying two-way measurement paths (see legend). Measurement temperature and relative humidity (RH) conditions varied very little from noon to 4PM at ~22°C and ~70%.
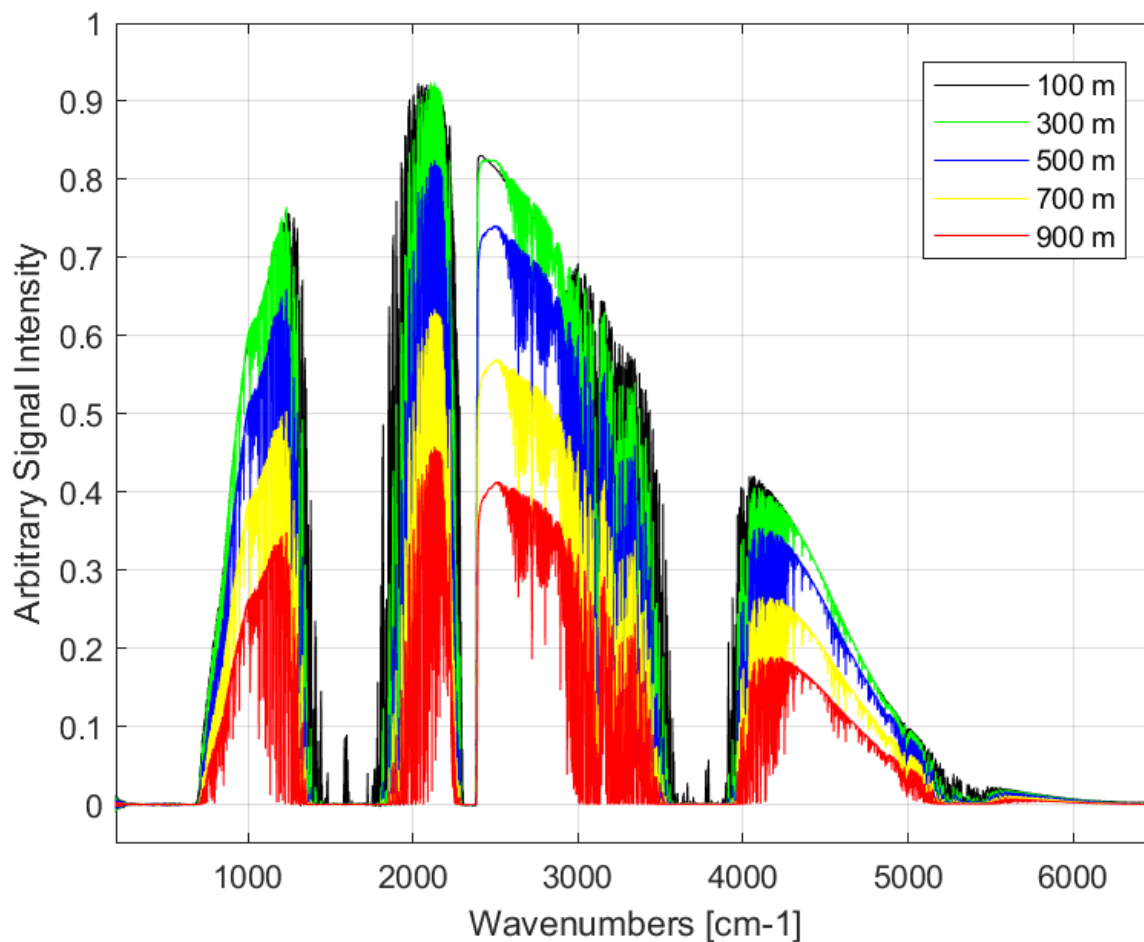
Figure 3.4. Raw spectra from Otter Lake (October, 2020), where a 50% larger array (89 cubes) was used at varying two-way measurements paths (see legend). Measurement temperature and RH conditions varied from ~21°C and ~60% RH at 2 PM to ~13°C and ~75% RH at 6 PM.
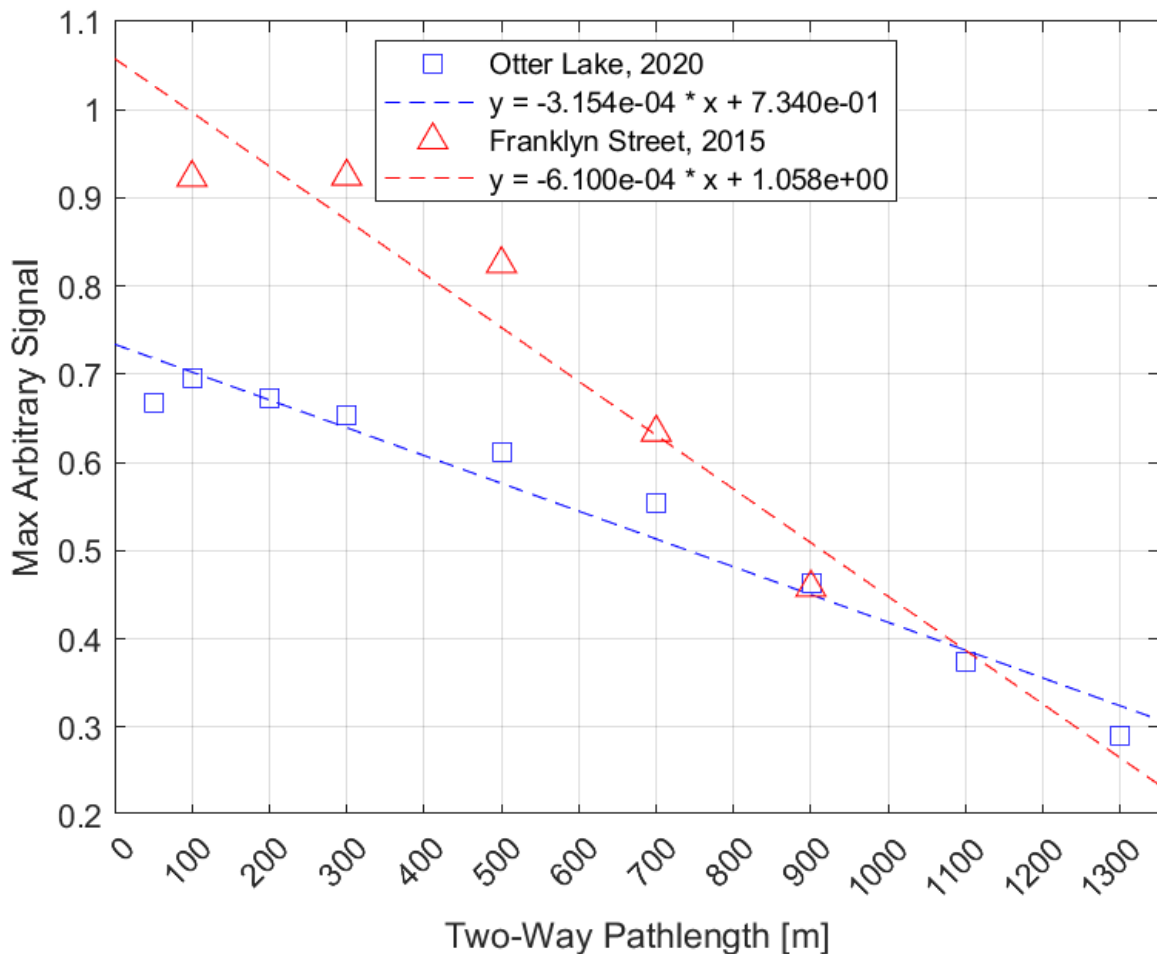
Figure 3.5. Maximum arbitrary signal intensity for varying two-way measurement path lengths in 2015 and 2020, together with lines of best fit.

In an experiment conducted across Halifax harbour in December 2020 (~570 m two-way), after the Otter Lake 2020, the pristine portion of the larger retroreflector array was covered to quantify its effect. Figure 3.6 shows eight spectra taken consecutively, with the first three spectra having the pristine portion of the array covered and the last four with the entire array exposed (one spectrum is affected by the removal of the covering). From these results, it is clear that the arbitrary signal

intensity in the 2000 cm^{-1} to 3000 cm^{-1} of the uncovered spectra are nearly twice the signal of the covered spectra. Thus the larger retroreflector array returns very nearly 100% more incoming radiation compared to the smaller retroreflector array, which is twice the increase expected based on the area increase (50%) alone, if all cubes had the same reflectivity. If we assume 100% reflectivity for the new cubes for simplicity, this implies that the old cubes have 50% "net" reflectivity, considering also that there are twice as many old cubes as new cubes. This assumes that the IR beam is uniform across all cubes, which is certainly not the case: In all likelihood the beam centre is aligned preferentially on the new, more reflective cubes, exaggerating somewhat the disparity between the reflectivity of the old and new cubes. Finally, we note that if the old cubes have a "net" reflectivity of 50%, this means that the degraded gold surface actually has a surface reflectivity of 70%, since two reflections of the beam take place in each cube.
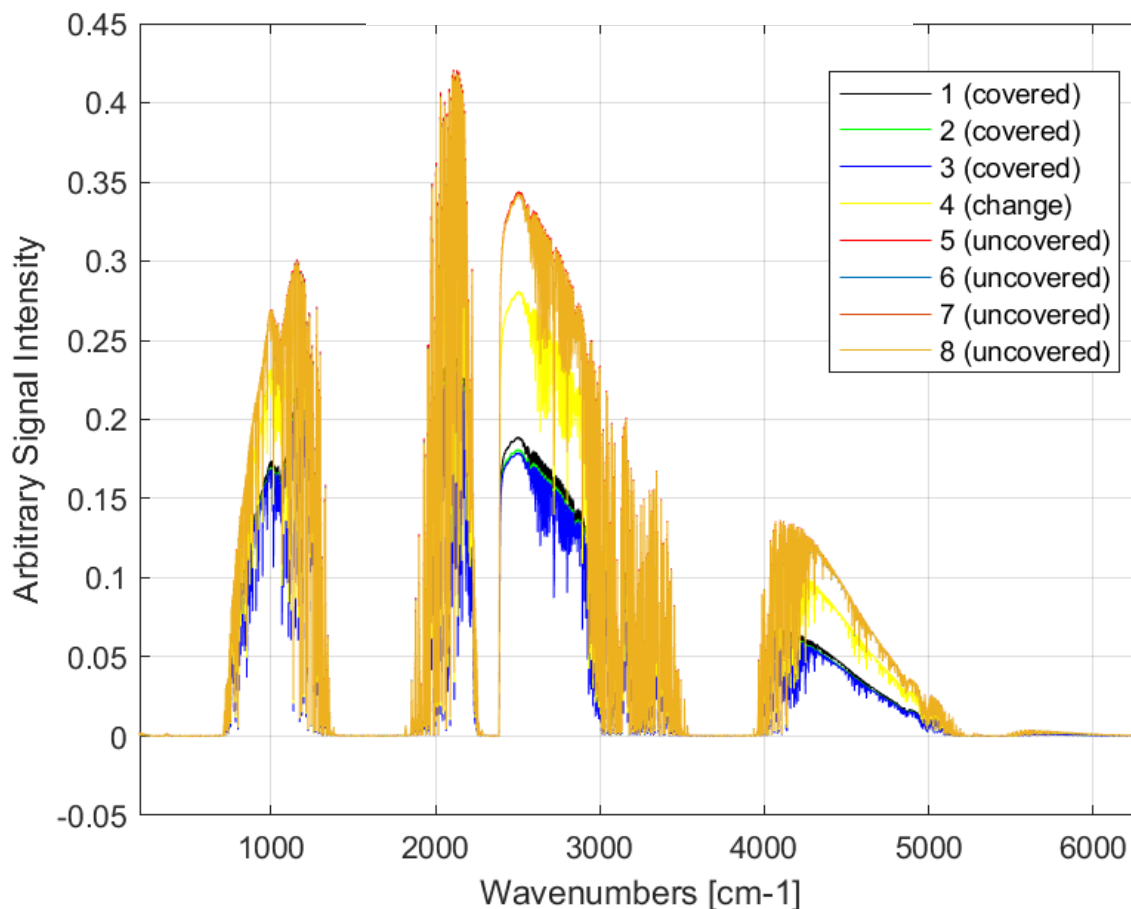
Figure 3.6: Spectra taken from Halifax harbour (~1100 m two-way), spectra 1-3 have the pristine cube corner retroreflectors covered, spectra 5-8 have the entire retroreflector array uncovered

3.2.2 Effect on Noise in Spectra

The spectral region used to estimate noise (see Section 2.2.3) is shown in Figure 3.7 (top) for the Otter Lake experiment. The signal remaining after normalization and de-trending has white noise characteristics and, upon closer examination (not shown), there are no

correlated spectral absorption features in this spectral region between spectra at different measurement paths. As expected, the longer paths, where the retroreflector is overfilled (and the return signal is being lost), exhibit higher noise values. The root-mean-square noise values estimated at both measurement locations are also shown in Figure 3.7 (bottom), and Otter Lake noise shows an increase of approximately one half the rate of Franklyn Street noise, based on the slopes of the lines of best fit (~4.8 m^{-1} vs. ~9.0 m^{-1}). Since the noise values are relative, it makes sense that they are higher at Otter Lake, where signal levels were lower, assuming constant instrumental noise.
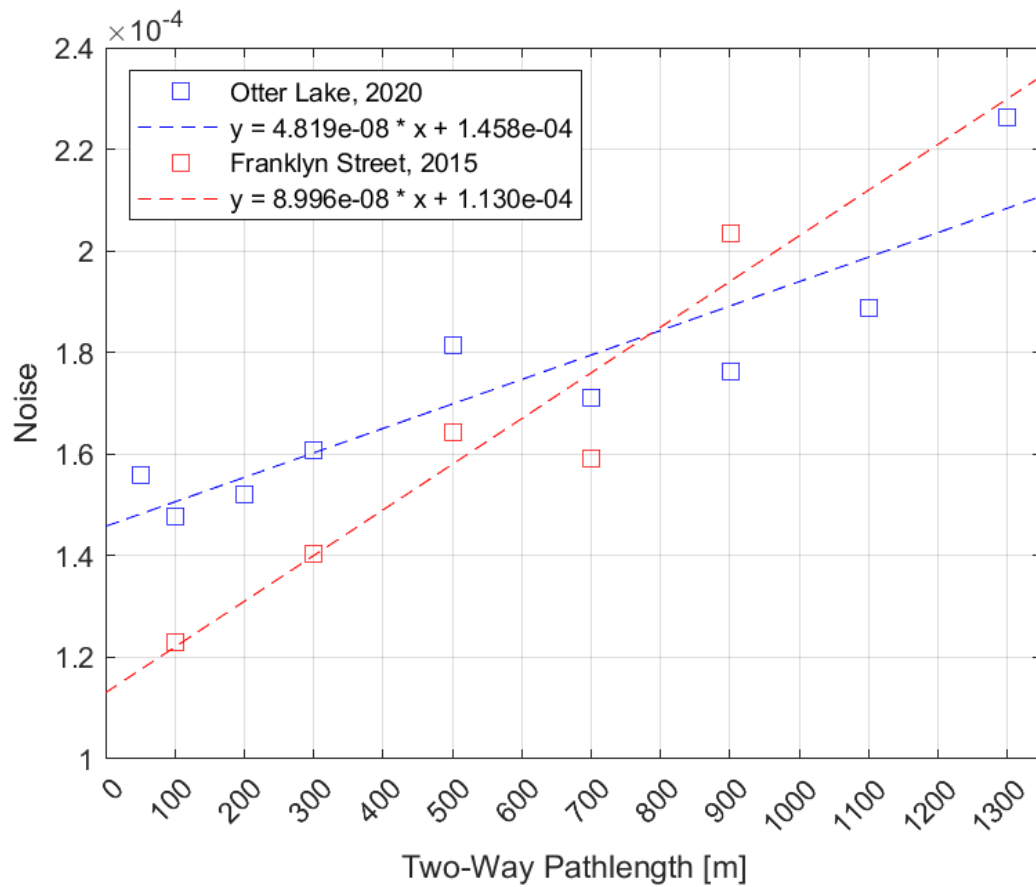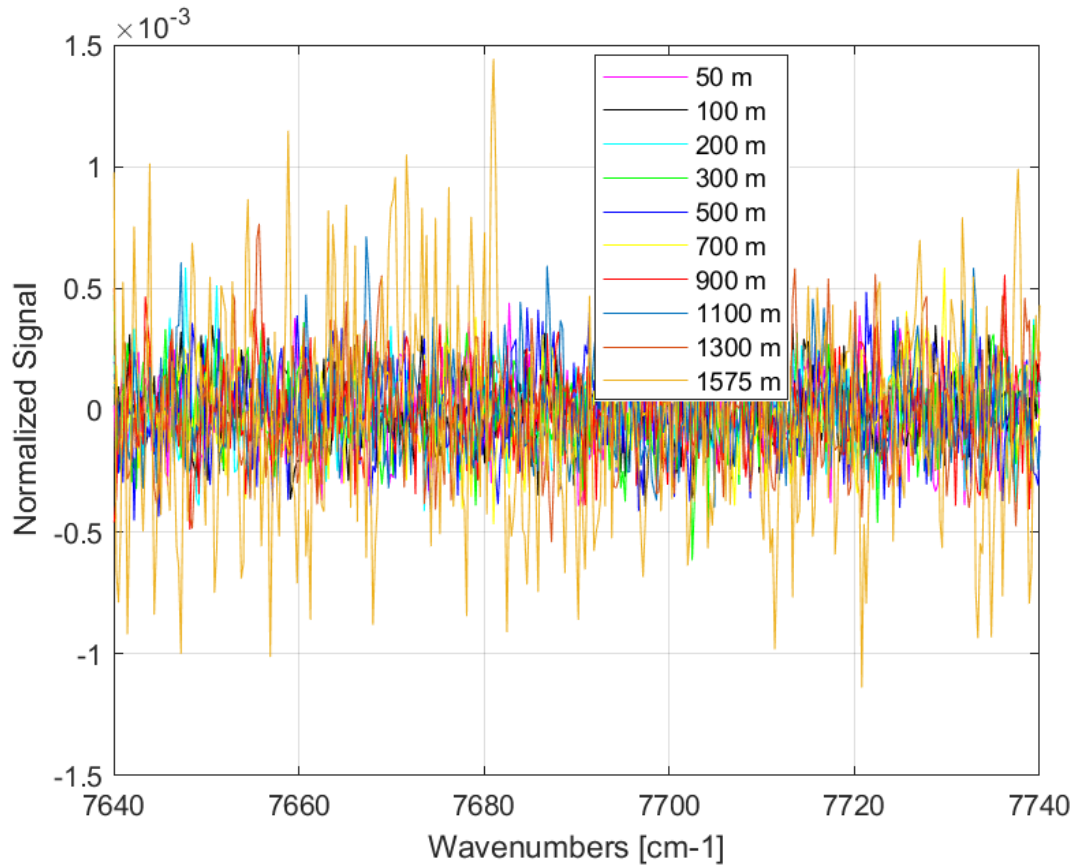
Figure 3.7: (top) Normalized and detrended spectral signatures in a region outside of instrumental response at Otter Lake (cf. Figure 3.4), which correspond to relative noise values. (bottom) RMS noise values at Franklyn Street (May 27, 2015, 59 cube corner retroreflector) and Otter Lake (October 16, 2020, 89 cube corner retroreflector), together with lines of best fit.

3.2.3 Effect on Signal and Noise

The signal-to-noise ratio of both experiments is shown in Figure 3.8. At short paths (e.g., 100 m) the higher signal in the 2015 Franklyn Street experiments leads to correspondingly higher SNR values, however, the Franklyn Street signal-to-noise ratio values decrease more than two times faster than the Otter Lake signal-to-noise ratio values with increasing paths ($\sim$ -1.5 m^{-1} vs. $\sim$ -3.6 m^{-1}). At long paths, i.e., 800 m and above, the Otter Lake experiment shows higher signal-to-noise ratio values.
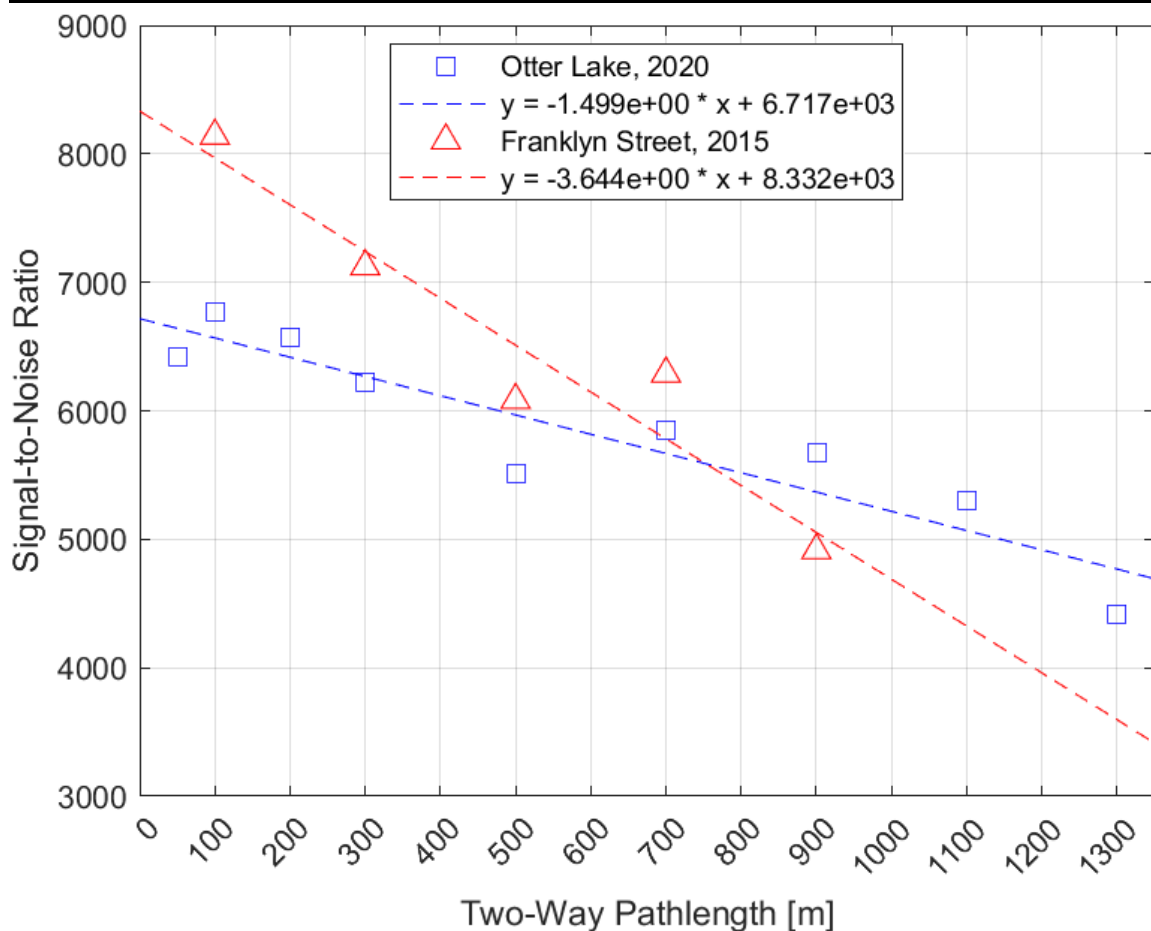
Figure 3.8: Signal-to-noise ratio for varying path lengths in 2015 (59 cube corner retroreflectors) and in 2020 (89 cube corner retroreflectors), together with lines of best fit.

3.2.4 Effect on Carbon Monoxide Retrieval

The effect of the measurement configuration and the resultant signal-to-noise on goodness-of-fit parameters for retrievals of carbon monoxide is shown in Figure 3.9. Carbon monoxide was chosen as a robust, easy to detect species.

Both experiments show increasing spectral fit root-mean-square (RMS) residuals with increasing path (Figure 3.9, top); however, whereas the noise for the Otter Lake experiment at 900 m was lower than that of the Franklyn Street noise (Figure 3.7, bottom) the corresponding residual value is higher than Franklyn Street. Systematic fitting effects act to increase the RMS fit residual above the random noise value. The fit residuals at 300 m and 900 m (Figure 3.10) for both experiments shows that the residuals for the Otter Lake experiments are greater than the Franklyn Street experiments, and that this has to do with systematic fitting errors of water.

Both experiments also show decreasing spectral fit percent errors with increasing path (Figure 3.9, bottom), which is consistent with increasing spectral absorption features of carbon monoxide with increasing path, as the absorption depth for both experiments is higher at a path of 900 m. At the highest path common to both experiments, the larger retroreflector array (Otter) shows a nearly identical percent error as the smaller retroreflector array (Franklyn). The absolute values of carbon monoxide retrieved are near background levels for Halifax in both experiments (within 135 ppb ± 10 ppb).
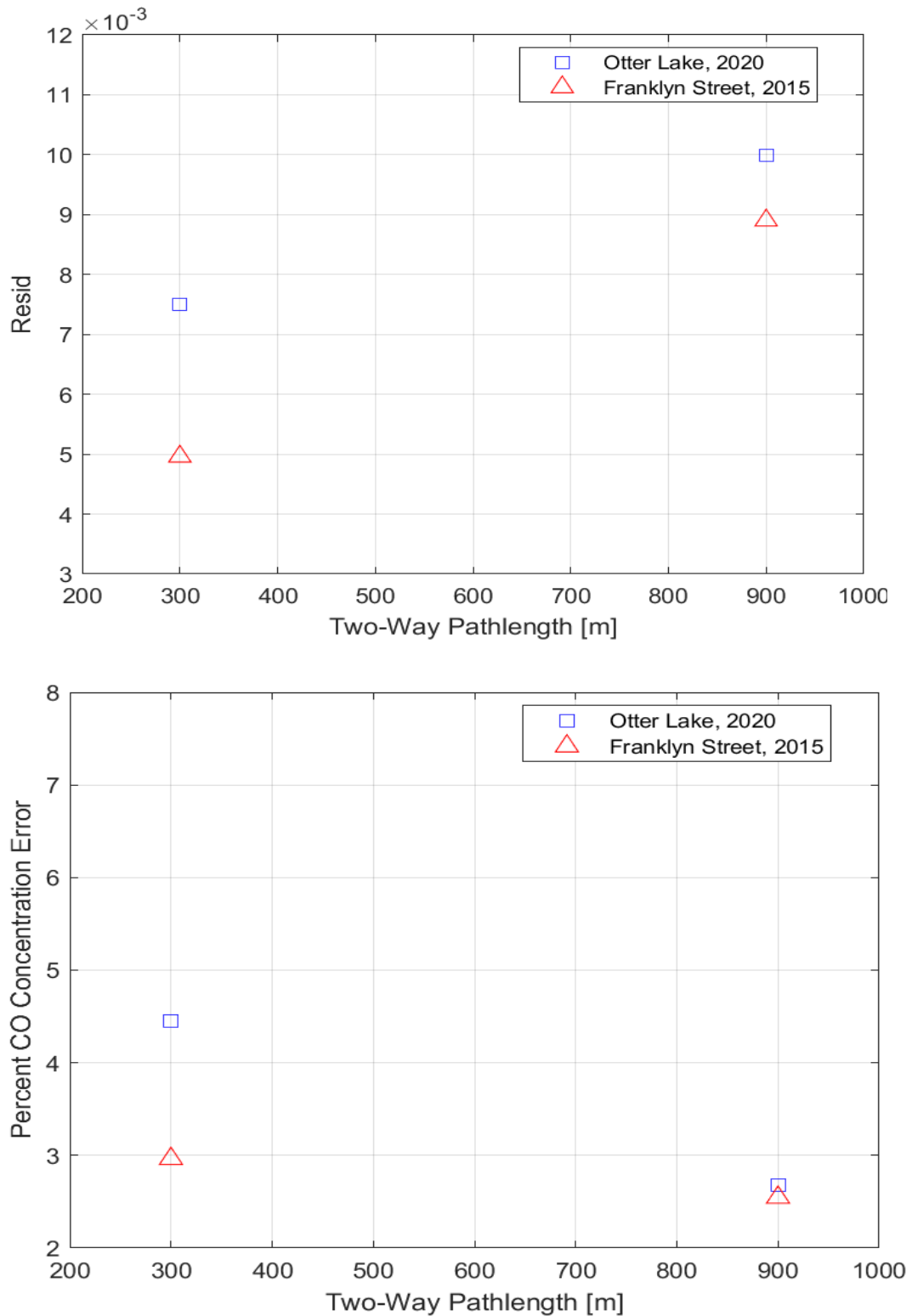
Figure 3.9: (top) Root-mean-square spectral fit residual for a carbon monoxide retrieval from a short path spectrum where the retroreflector is not overfilled and from a spectrum at the longest path length common to both experiments. (bottom) Retrieved carbon monoxide concentration percent error for the same spectral retrievals.
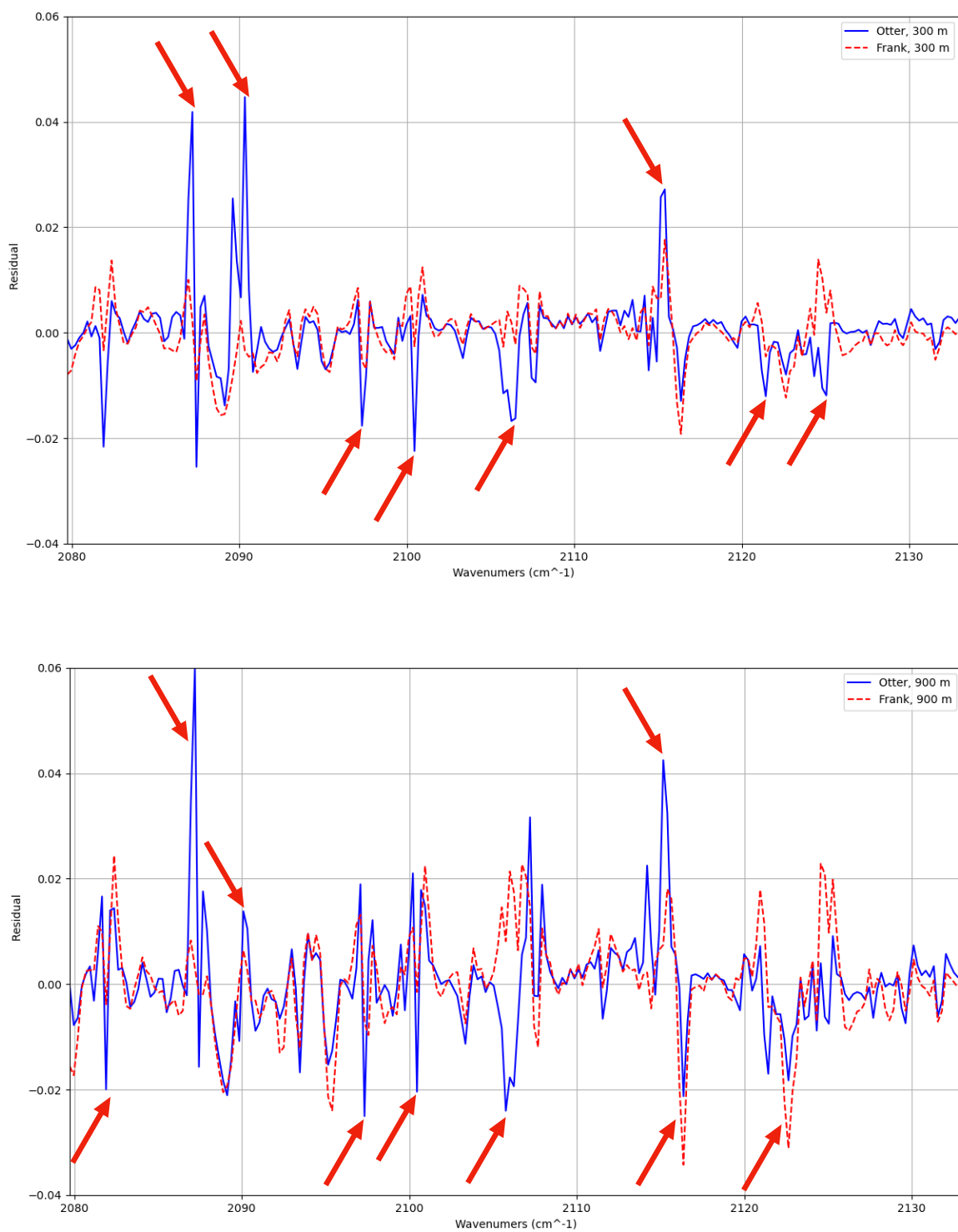
Figure 3.10: Carbon monoxide fit residuals for Otter Lake and Franklyn Street for a path difference of 300 m (top) and 900 m (bottom). Arrows point out residual features due to water misfitting

3.3 Theoretical Spectral Simulations

For the theoretical spectral simulations in this project, ~10 target gases were selected, also in multiple spectral windows for certain gases. In the following sections, carbon monoxide and formaldehyde will be discussed in detail, while the results for the other gases are shown in Appendix B. Carbon monoxide was chosen due to its abundance, ease of detection, as well as previous work, while formaldehyde was selected due to its comparatively small abundance and difficulty of detection, molecular complexity, and importance in air quality.

3.3.1 Percent Absorption vs. Path

In Figure 3.11 the effect of increasing path length (which starts at 50 m and increases up to 1500 m in 50 m increments) on the absorption spectrum of the target and interfering gases is shown. Figure 3.11 (top) shows that the percent absorption of carbon monoxide and interfering gases increases with increasing path length, peaking at ~100%, due to water vapour absorption. These regions of water saturation do not carry information about other trace gas concentrations, as an infinity of

mathematical solutions exists for other trace gases overlapped by 100% water absorption. The best region to perform carbon monoxide retrievals is between 2100 cm^{-1} to 2200 cm^{-1}, as it avoids regions of 100% absorption. Additionally Figure 3.11 (top) shows that at short path lengths (< ~500 m), the percent absorption of regions without water lines (such as at approximately 2120 cm^{-1} and 2170 cm^{-1}) is ~20%, with only a fraction of that percentage coming from carbon monoxide (Figure 3.12 (top)), thus further complicating detection.

Figure 3.11 (bottom), shows that the peak absorption is ~55%, corresponding to water features at approximately 2720 cm^{-1}. It can also be seen that the percent absorption increases with increasing path length, with shorter path lengths (< ~400 m) reaching only ~15% absorption. This means that retrievals are theoretically better at longer path lengths, as the higher percent absorption indicates that more of the target gas spectral signature is present, however, this percent absorption includes the interfering gases in Figure 3.11. To discern how the target gas impacts this percent absorption, the differential absorption plots in Section 3.3.2 are more informative.
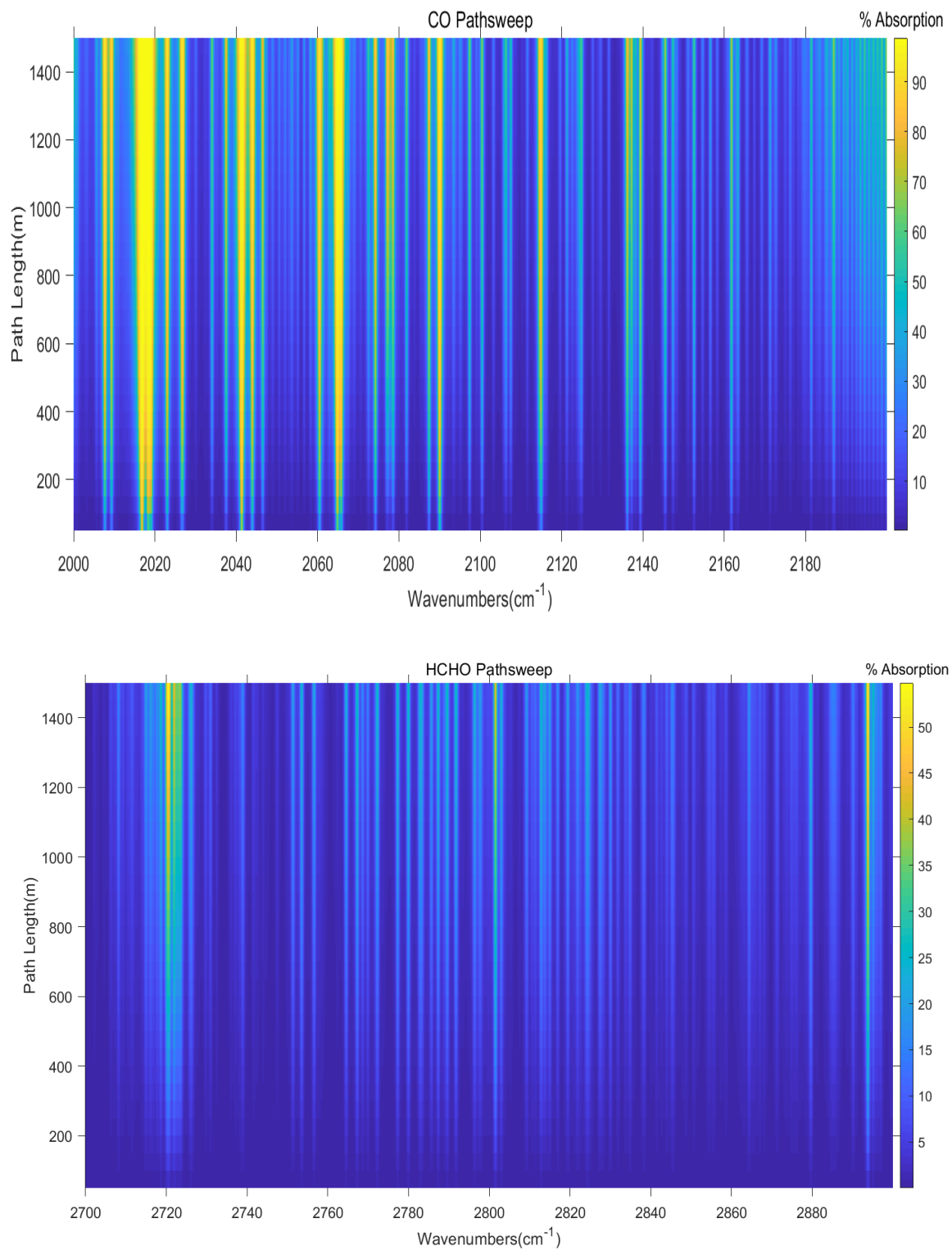
Figure 3.11: (top) Percent absorption due to 130 ppb carbon monoxide and interfering species as a function of varying path. (bottom) Percent absorption due to 1 ppb formaldehyde and interfering species as a function of varying path.

3.3.2 Differential Absorption

Figure 3.12 shows a set of transmittance spectra, which includes the target and inferring gases, plotted above a differential absorption spectrum. This is to help relate the spectral features of the selected gases to the corresponding features in the differential absorption plot. Figure 3.12 (top), shows that the spectral lines in the transmittance spectrum of carbon monoxide, which reach a minimum of ~0.80, correspond to lines of increased differential absorption, peaking at ~ 20%. From these differential lines, it is clear that the differential absorption of carbon monoxide increases as path length increases. This implies that the best path length to measure carbon monoxide is the longest path length possible for the OP-FTIR system, provided that overfilling of the retroreflector does not result in a signal-to-noise ratio unsuitable for measurements, as shown in Section 3.2.3, Figure 3.8.

In Figure 3.12 (bottom), the transmittance spectrum is zoomed in to see the spectral features of formaldehyde, which only reaches a minimum transmittance of ~0.9985. It is clear that very short path lengths (< ~300 m) provide an approximate differential percent absorption of < 0.06%, which is technically large enough for

formaldehyde to be detected in the presence of the interfering gases, because the noise is 0.014 - 0.016% (Figure 3.7) at these separations. The differential percent absorption of formaldehyde alone reaches a maximum of only ~0.12% at the maximum path length of 1500 m, which is also technically higher than the random noise of ~0.025% at these separations (Figure 3.7). This means that at longer path lengths the interfering gases are not obscuring the target gas, as the pink differential absorption bands intensify toward maximum path difference. However, it must be noted that this analysis considers random noise only, and that systematic noise due to spectroscopic parameter errors is always an issue in fit residuals, as discussed later. For robust detection to be possible, the individual yet spectrally correlated contributions from the target gas features must be comparable to the noise of the retrieval, which includes both random and systematic components.

Certain species can be obscured by the interfering gases at a certain threshold path difference, giving diminishing returns in detection limits at increasing path lengths. One example of a species that shows this behaviour is nitric oxide ($1560 \; cm^{-1}$ - $1660 \; cm^{-1}$), region

shown in Figure 3.13. It is clear that the largest differential percent absorption is present in the lines centred around $\sim$1585 cm^{-1}, 1600 cm^{-1}, and 1605 cm^{-1}. Each of these regions show diminishing returns as the path length increases, with the lines at $\sim$1585 cm^{-1} and 1605 cm^{-1} extinguishing before the maximum path, while the lines near 1600 cm^{-1} begin to narrow at a path difference of approximately 500 m. As stated above, this occurs as a result of interfering gases dominating over the target gas at longer path lengths.
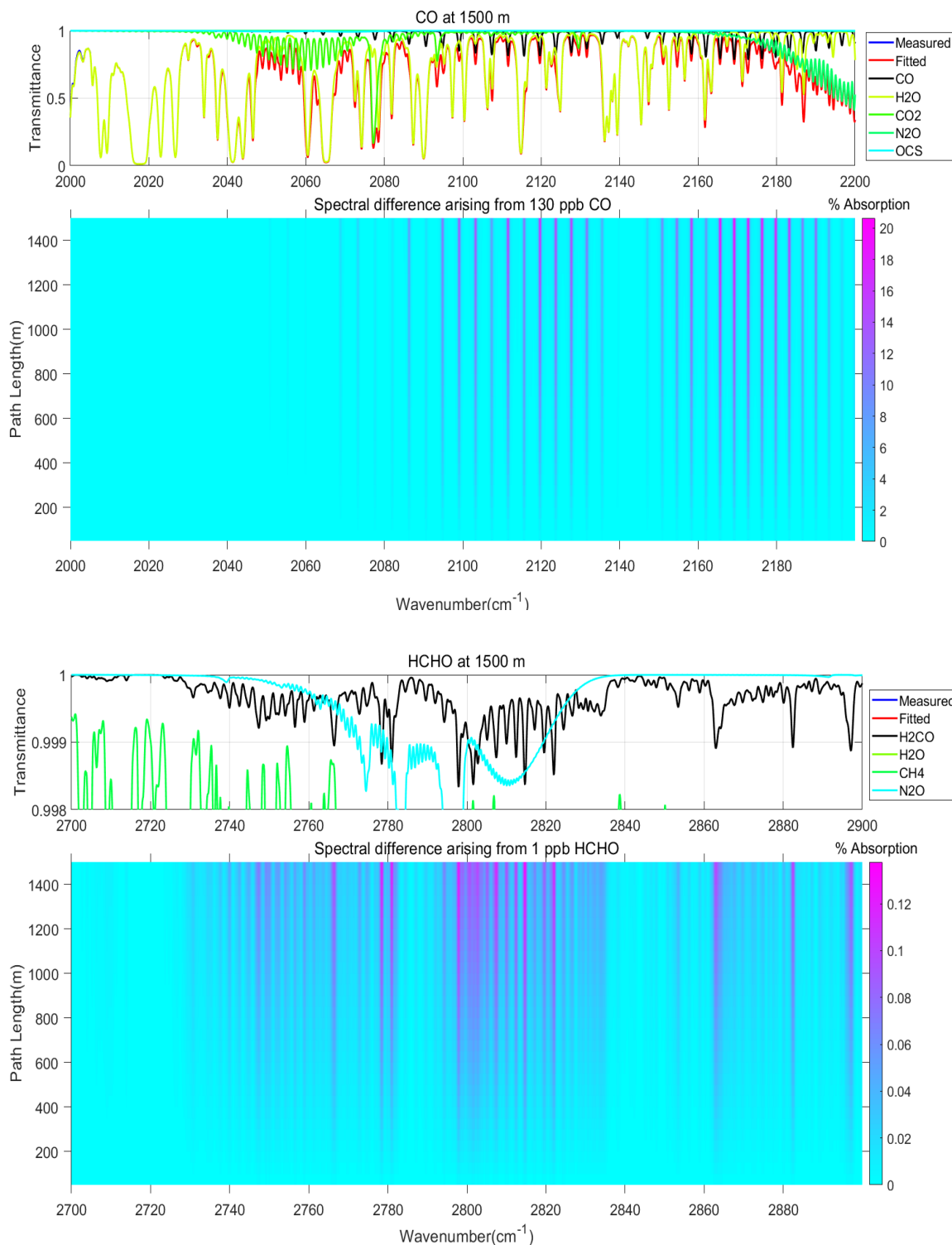
Figure 3.12: (top) Differential absorption due to 130 ppb carbon monoxide in the presence of interfering gases as a function of varying path and corresponding transmittance spectrum for target and interfering gases. (bottom) Differential absorption due to 1 ppb formaldehyde in the presence of interfering gases as a function of varying path and corresponding transmittance spectrum for target and interfering gases.
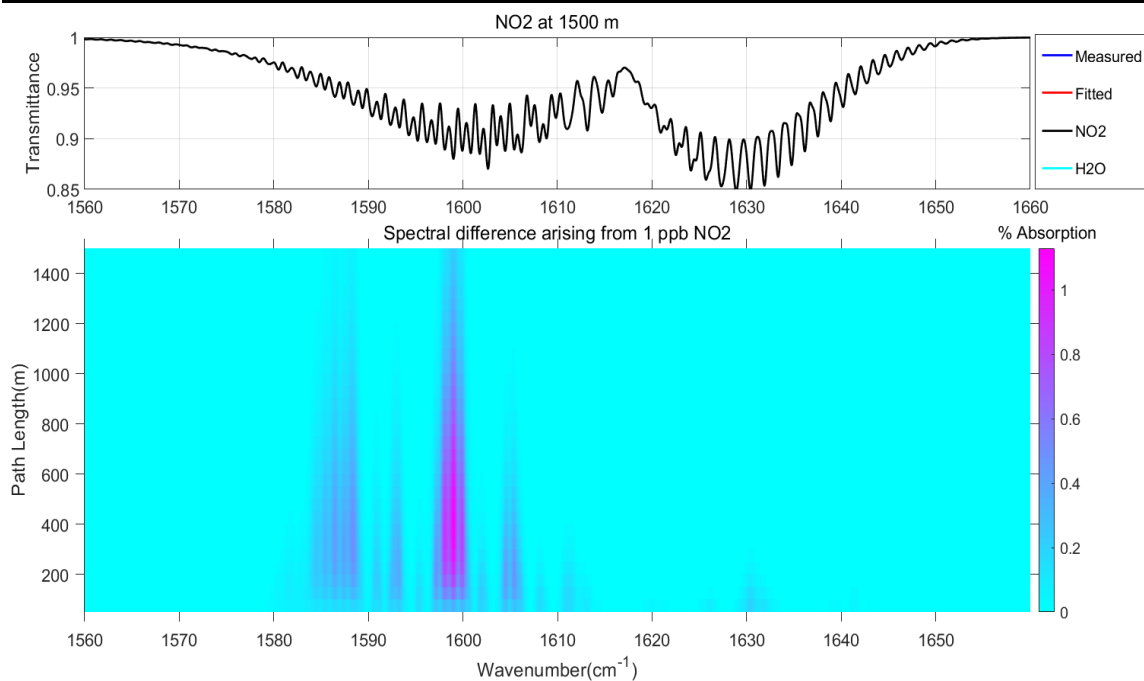
Figure 3.13: Differential absorption due to 25 ppb nitric oxide in the presence of interfering gases as a function of varying path and corresponding transmittance spectrum for target and interfering gases.

3.3.3 Increasing Target Gas Concentration

To examine the relationship between absorbance, which is proportional to concentration, and transmittance which is logarithmically related to absorbance, simulations of carbon monoxide and formaldehyde were conducted with initial concentrations at ten times the typical values (1300 ppb and 10 ppb respectively). The differential absorption of carbon monoxide and formaldehyde are shown in Figure 3.14 (top and bottom respectively); note that all other input parameters remain identical to the parameters used in the

simulations shown in Section 3.3.2. Additionally, the y-axis of the transmittance spectra has been rescaled to show the spectral features of the target gases.

The maximum differential percent absorption due to carbon monoxide in Figure 3.14 (top) is ~60%, which has increased by a factor three as compared to Figure 3.12 (top). This is despite the carbon monoxide concentration increase by a factor of ten, highlighting the non-linear relationship between transmittance and absorbance (see Figure 1.4). This is not the case for formaldehyde, in Figure 3.14 (bottom), which shows an increase of a factor of ten in percent difference as compared to Figure 3.12 (bottom). These same factors are also present in minimum transmittance subtract one for each target gas, which represents absorption. From Figure 3.15 it is clear that carbon monoxide and formaldehyde exhibit different behaviour when the concentration is increased due to their location on the solid curve. Thus for species with a low background concentration of ~ 1 ppb, such as formaldehyde, concentration increases appear in a linear region of Figure 3.15, while more abundant gases, such as carbon monoxide, do not.
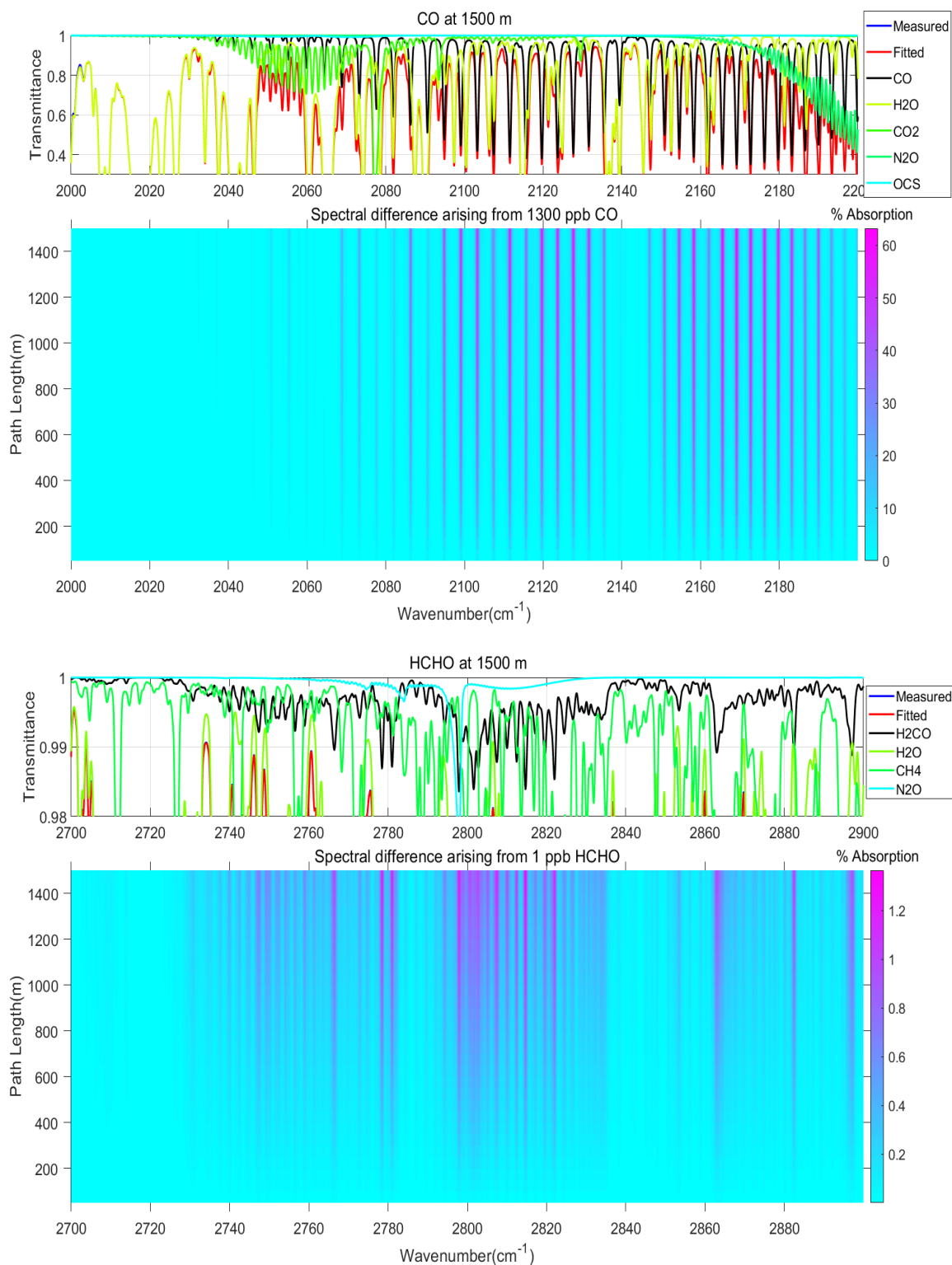
Figure 3.14: (top) Differential absorption due to 1300 ppb carbon monoxide in the presence of interfering gases as a function of varying path and corresponding transmittance spectrum for target and interfering gases. (bottom) Differential absorption due to 10 ppb formaldehyde in the presence of interfering gases as a function of varying path and corresponding transmittance spectrum for target and interfering gases.
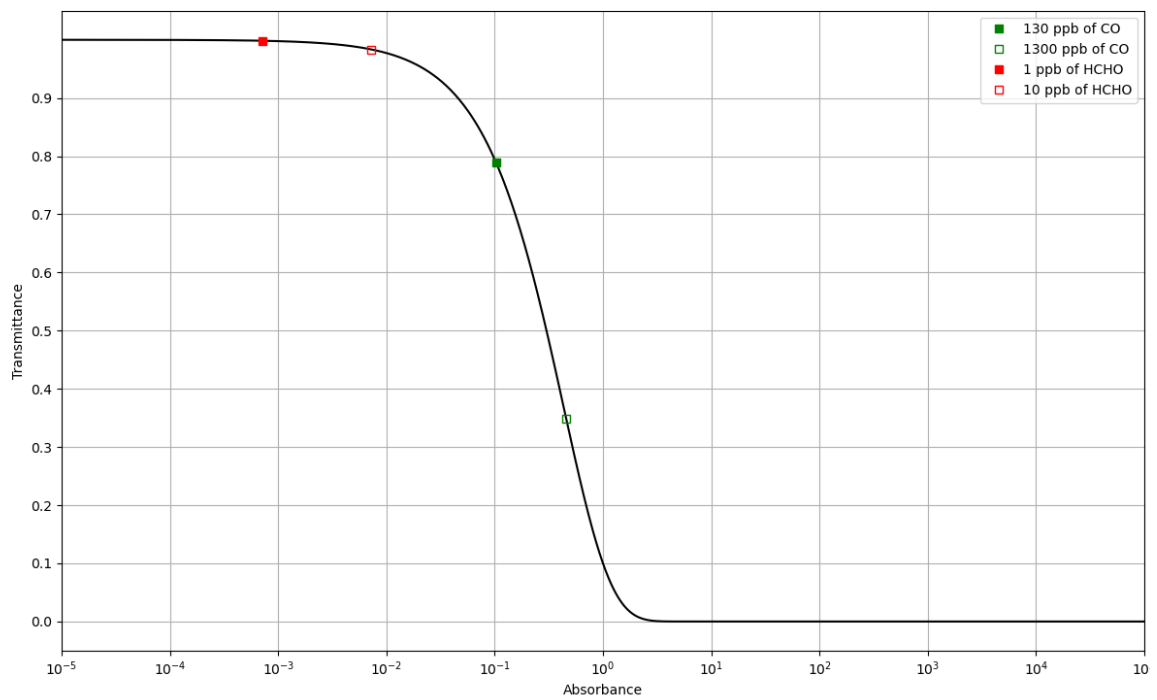
Figure 3.15: Logarithmic relationship between transmittance vs absorbance with gases from Sections 3.2 and 3.3. Note that transmittance are taken from a simulation at 1500 m.

Chapter 4

Conclusions and Future Work

Setting out, the goals of this project were, 1) to characterize the effects of retroreflector array cleaning and size, 2) to determine how parameters such path length, (interfering) water concentration, and target concentration affect the differential absorption of a target gas through simulations, and 3) to determine the effects of increases in the target gas concentration, also through simulations.

The effect of the retroreflector cleaning was found to be a modest signal increase of 10%, with no visible effects on array appearance. After a surface characterization of one cube corner retroreflector was performed by Dr. Hanley, his findings were that the aluminum-chromium alloy substrate holding the gold mirror coating is heavily surface oxidized/corroded, producing the principal visible contaminant of aluminum-hydroxide. These contaminants are only present in

significant thickness on the outermost 500 *µm* of the surface, near the mirror edge, corresponding to the area of visible contamination. For the outermost 500 *µm* to 3 mm of the altered, buckled window, the total reflectivity is estimated to be close to 100%. The total signal loss, which is correlated to the optical area, was estimated (over all 3 mirrors of this heavily impacted cube) to be no more than 3%, which accounts for gold buckling and contamination. This, however, is lower than other independent estimates of signal loss of 15-25% over the entire array area, including a 10% contribution from source intensity changes, and points to reflectivity losses in areas without visible contaminants, as may be expected due to the presence of organic and inorganic thin coatings.

From experiments conducted with the larger retroreflector array, it was determined that the signal-to-noise ratio for the experiment with the larger retroreflector array decreased as a function of array-spectrometer separation at half the rate of the experiment with the smaller retroreflector. This directly correlated to the behaviour of the noise in the two experiments, as the noise of the larger retroreflector experiment increased at half the rate of the smaller retroreflector experiment, again, as a function of array-spectrometer separation.

From the raw spectra taken from both experiments, it is clear that the peak arbitrary signal levels were higher for the smaller retroreflector array experiments by approximately 25%. This may be accounted for by considering the impact of the older cube corner retroreflectors as well as the intensity decrease of the Globar infrared source used by the spectrometer. Looking at spectra taken with and without the pristine portion of the larger retroreflector array showed that the returning arbitrary signal levels are approximately doubled with the larger retroreflector.

From absorption and differential absorption plots of carbon monoxide, it can be seen that the retrievals should be conducted between 2100 cm^{-1} to 2200 cm^{-1}, preferably at larger path lengths. For formaldehyde, path lengths of ~300 m and shorter do not have the absorption required to detect formaldehyde when systematic sources of error are taken into consideration in spectral residuals. Lastly, for trace gases with typical concentrations of ~1 ppb, such as formaldehyde, differential absorption and absorbance are approximately linearly related, while trace gases with more abundant background values, such as carbon monoxide at ~130 ppb, this relation is non-linear.

To further analyze the effect of the larger retroreflector array, measurements can be taken at locations where the smaller retroreflector array was recently used. These results can then be cross-referenced with more recent results from the smaller retroreflector array (earlier than the 2020 Otter Lake experiments). Next in future work, the gases shown in Section 3.2 and Appendix B are all taken from the HITRAN database, however, more complex species can be simulated using a database such as the Pacific Northwest National Lab. In the future, the current code used for these simulations can be updated to include more complex species. Additionally, the output figures shown in Section 3.2 and 3.3 are simulated at a higher resolution then is capable for most OP-FTIR systems. Future work should address this issue by implementing a resolution setting into the code used for simulations. Finally, all the simulated species should be plotted on Figure 3.15 since their absorbance is a function of a combination of concentration, absorption cross-section, and path length; as such, concentration alone does not predict a species' location on Figure 3.15.

Appendix A

List of input parameters required to perform spectral simulations

Simulation Parameter	Carbon Monoxide	Formaldehyde
Spectral Window	2000 cm^{-1} - 2200 cm^{-1}	2700 cm^{-1} - 2900 cm^{-1}
Pressure	1013.25 mb	1013.25 mb
Temperature	15 ^{o}C	15 ^{o}C
Path length	50 m - 1500 m	50 m - 1500 m
Step	50 m	50 m
Target gas concentration	130 ppb	1 ppb
Interferring gases	Water (1%) Carbon dioxide (400 ppm) Nitrous oxide (330 ppb) Carbonyl sulphide (0.5 ppb)	Water (1%) Methane (2 ppm) Nitrous oxide (330 ppb)

Appendix B
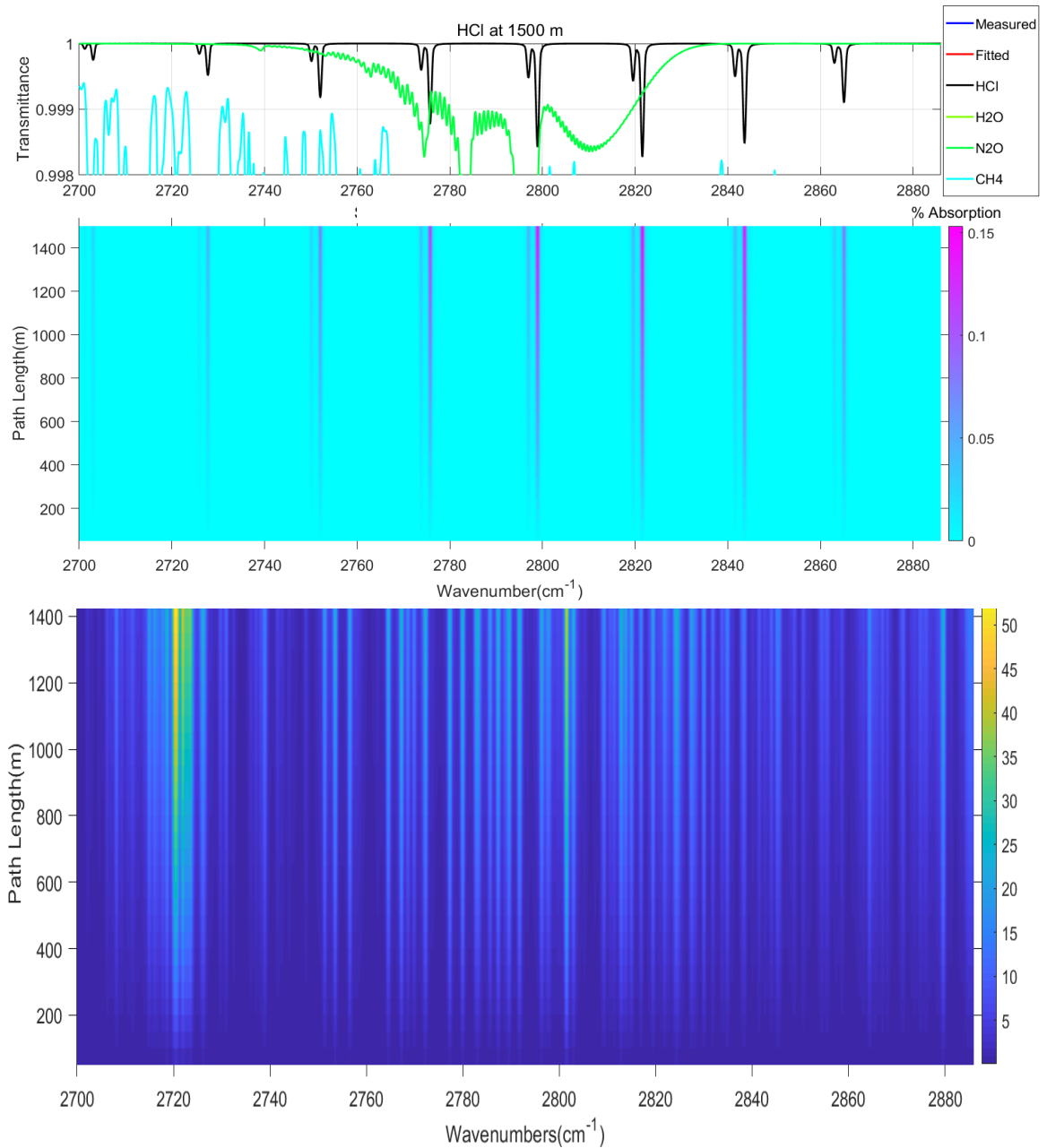
Figure 1: (top) Differential absorption due to 1 ppb hydrogen chloride in the presence of interfering gases as a function of varying path and corresponding transmittance spectrum for target and interfering gases. (bottom) Percent absorption due to 1 ppb hydrogen chloride and interfering species as a function of varying path and corresponding transmittance spectrum for target and interfering gases.
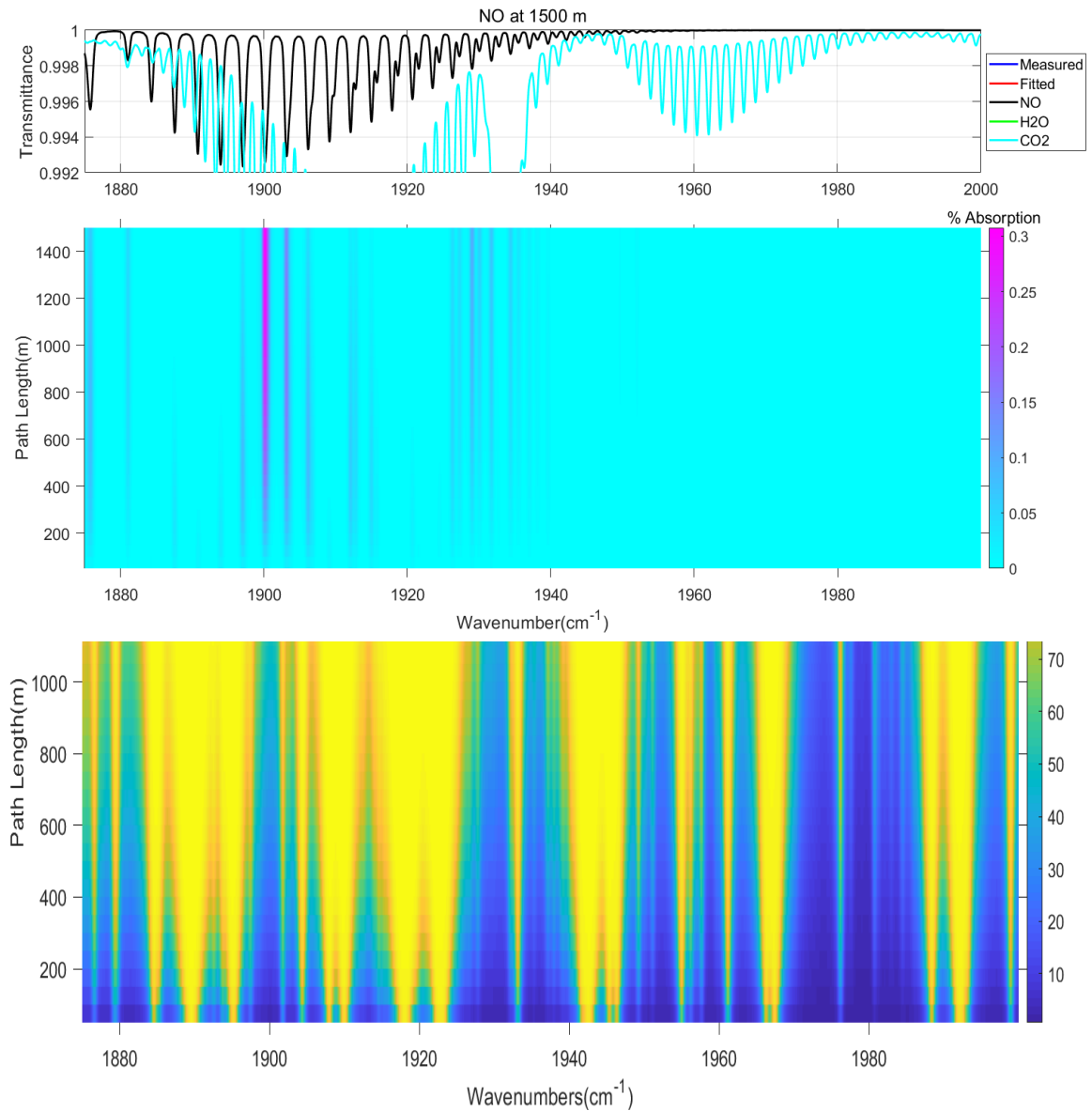
Figure 2: (top) Differential absorption due to 1 ppb nitrogen dioxide in the presence of interfering gases as a function of varying path and corresponding transmittance spectrum for target and interfering gases. (bottom) Percent absorption due to 1 ppb nitrogen dioxide and interfering species as a function of varying path and corresponding transmittance spectrum for target and interfering gases.
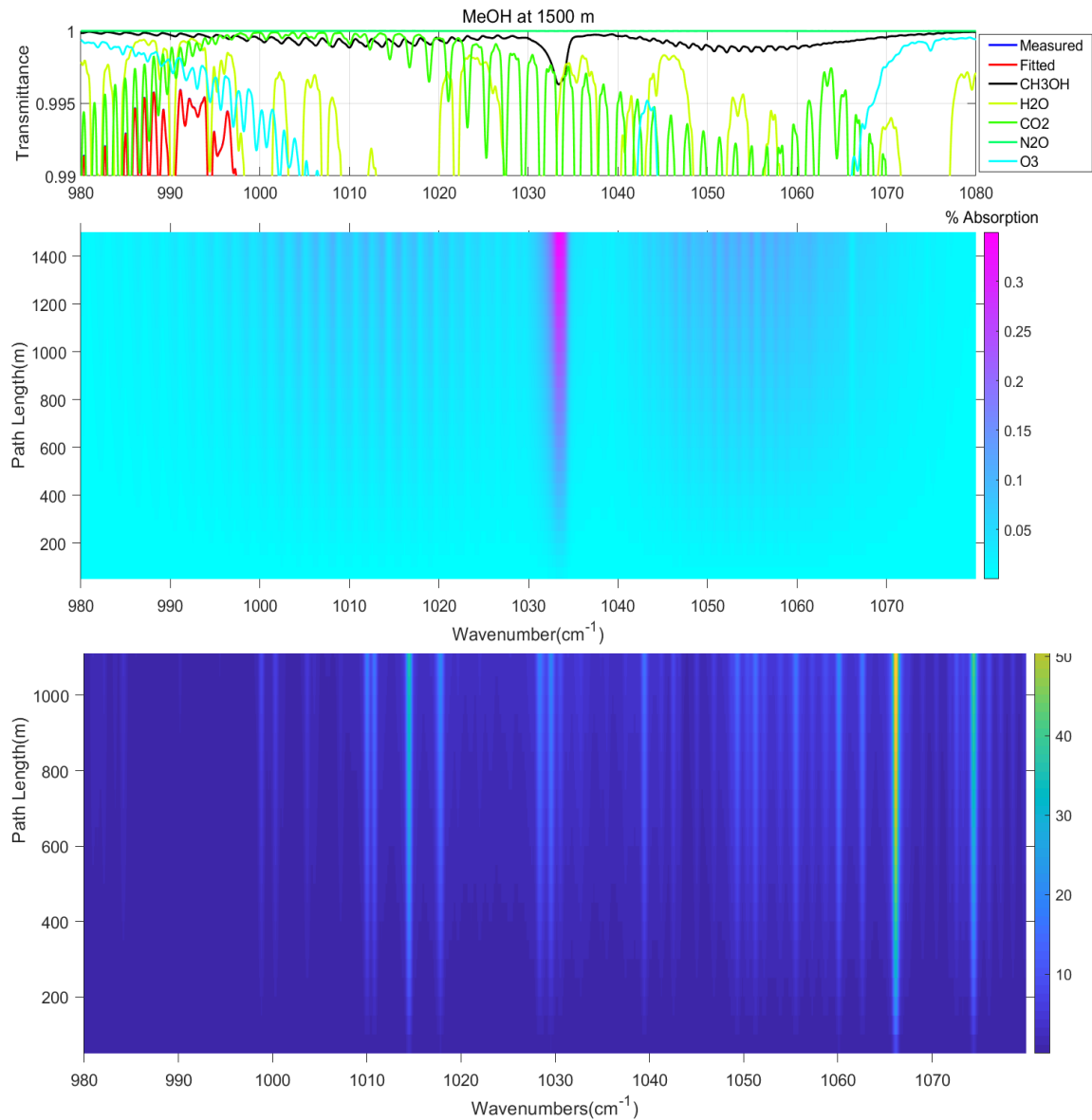
Figure 3: (top) Differential absorption due to 1 ppb methanol in the presence of interfering gases as a function of varying path and corresponding transmittance spectrum for target and interfering gases. (bottom) Percent absorption due to 1 ppb methanol and interfering species as a function of varying path and corresponding transmittance spectrum for target and interfering gases.
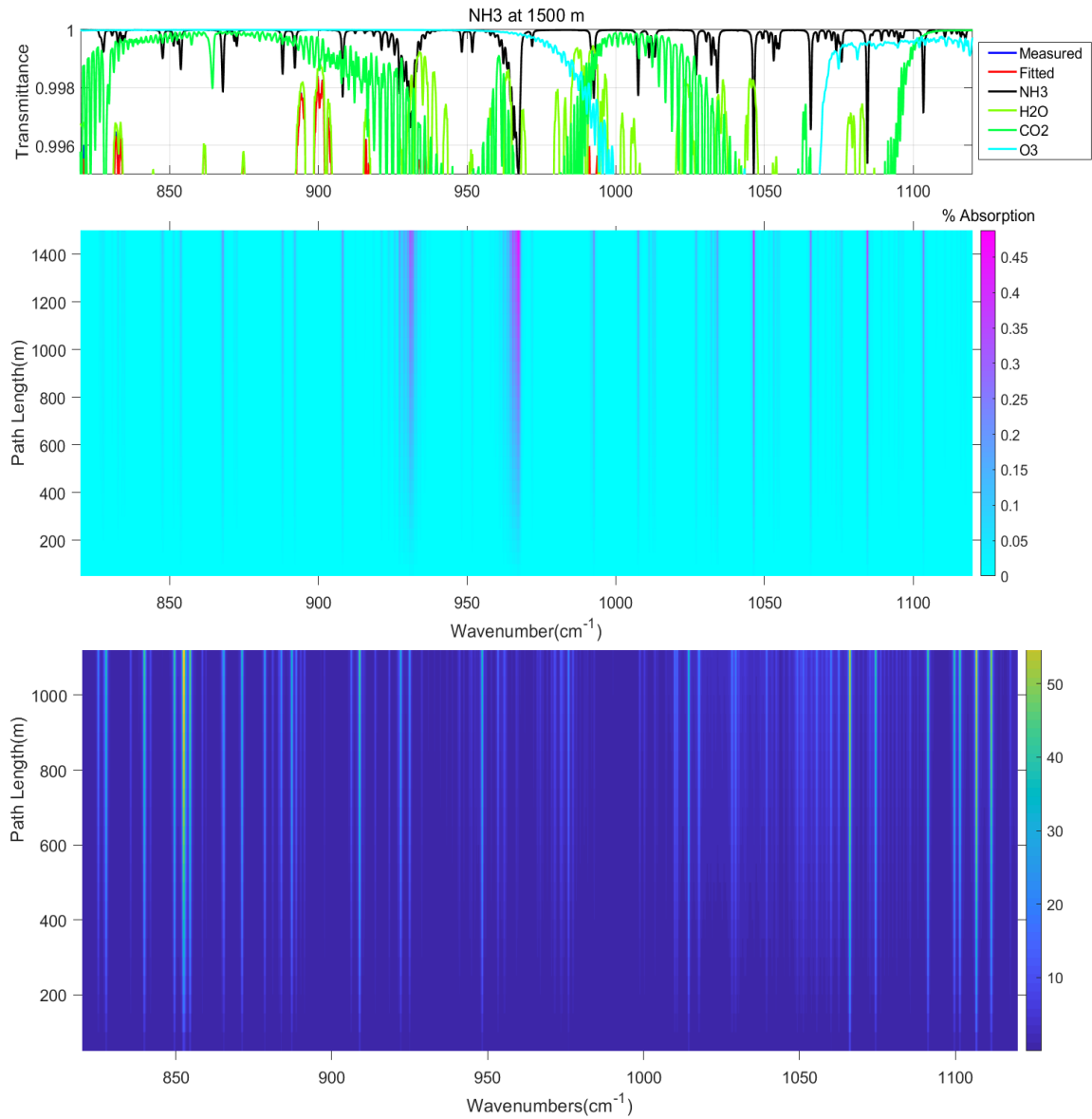
Figure 4: (top) Differential absorption due to 1 ppb ammonia in the presence of interfering gases as a function of varying path and corresponding transmittance spectrum for target and interfering gases. (bottom) Percent absorption due to 1 ppb ammonia and interfering species as a function of varying path and corresponding transmittance spectrum for target and interfering gases.
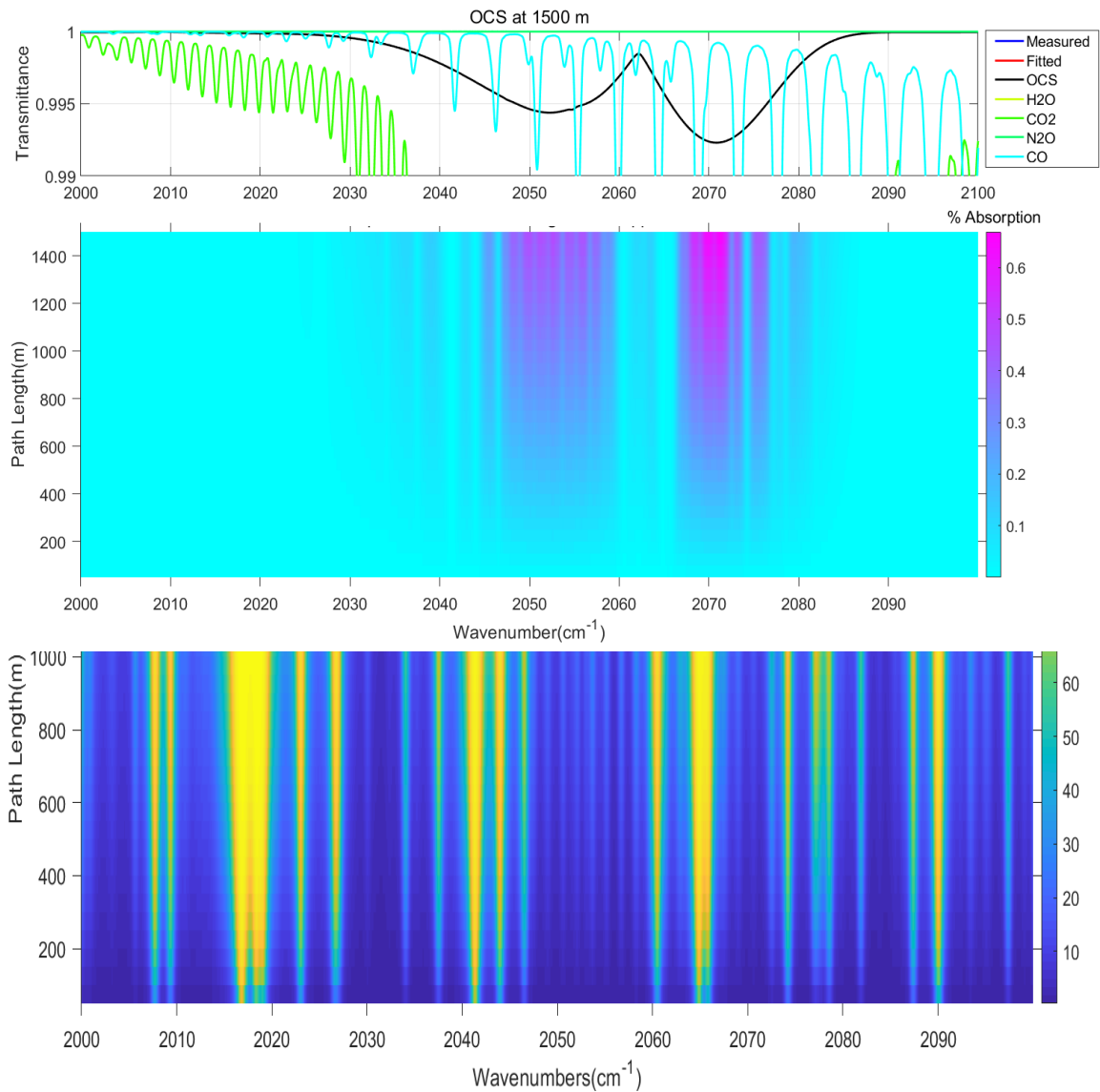
Figure 5: (top) Differential absorption due to 0.5 ppb carbonyl sulphide in the presence of interfering gases as a function of varying path and corresponding transmittance spectrum for target and interfering gases. (bottom) Percent absorption due to 0.5 ppb carbonyl sulphide and interfering species as a function of varying path and corresponding transmittance spectrum for target and interfering gases.
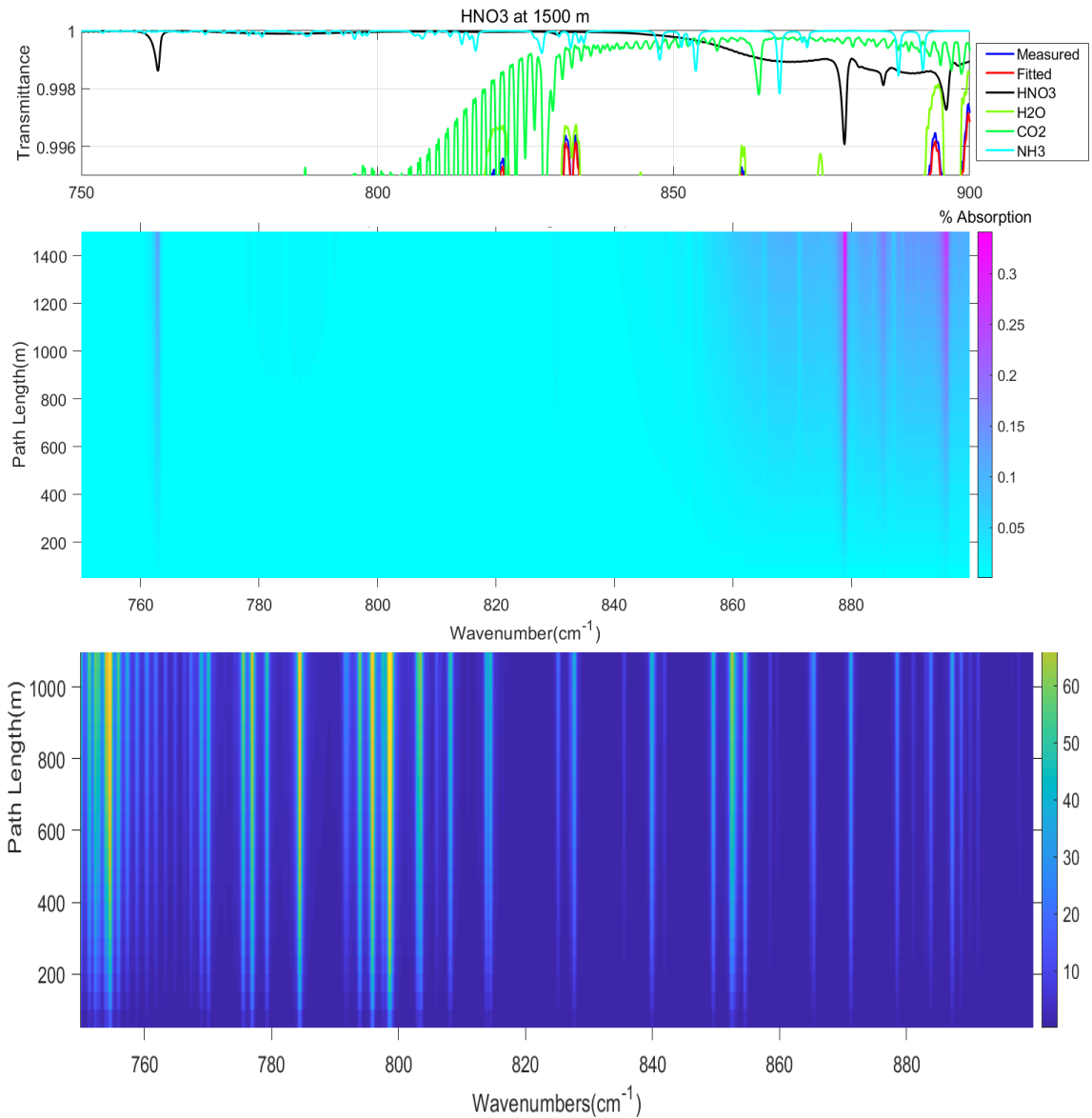
Figure 6: (top) Differential absorption due to 1 ppb nitric acid in the presence of interfering gases as a function of varying path and corresponding transmittance spectrum for target and interfering gases. (bottom) Percent absorption due to 1 ppb nitric acid and interfering species as a function of varying path and corresponding transmittance spectrum for target and interfering gases.
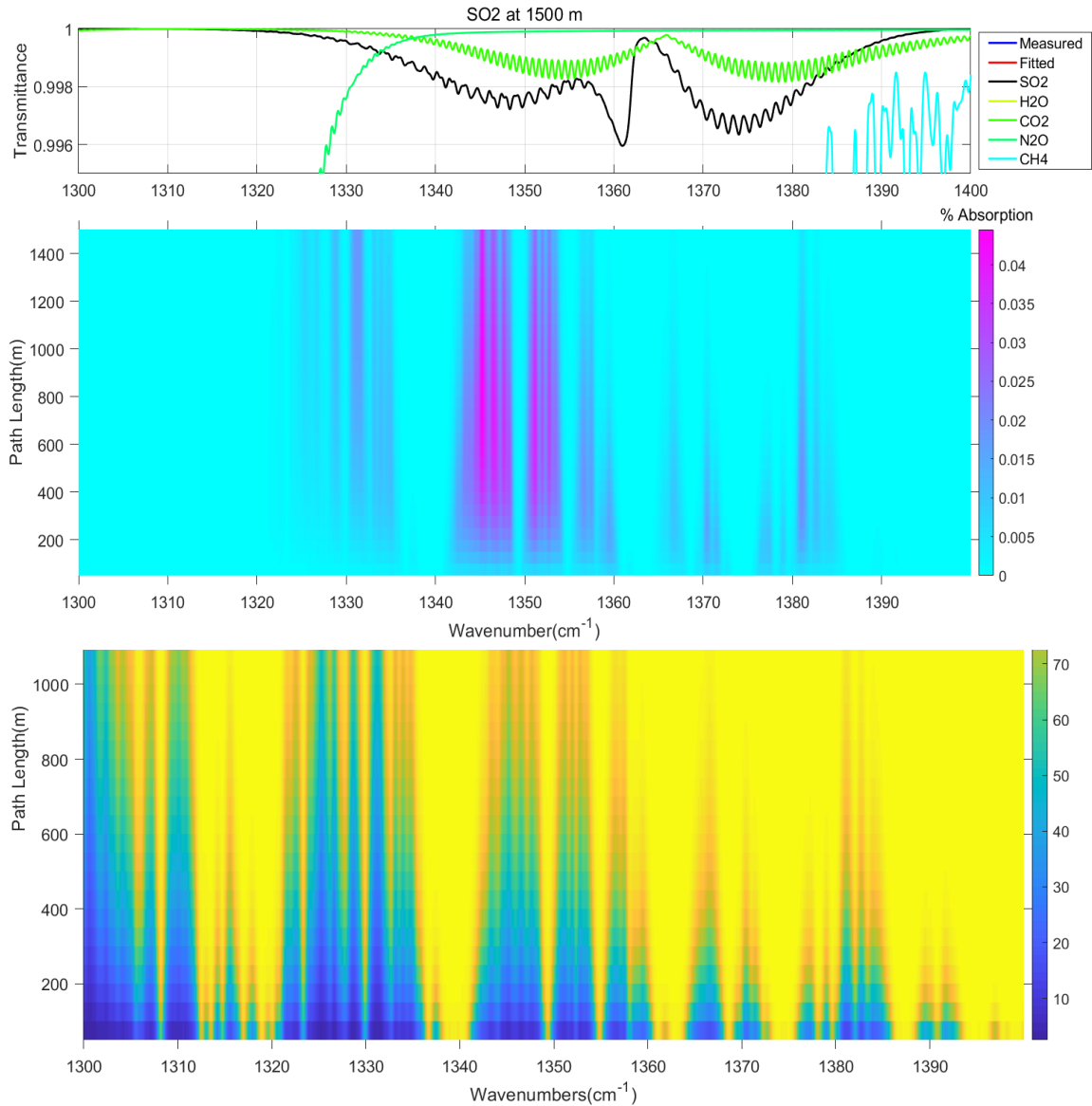
Figure 7: (top) Differential absorption due to 1 ppb sulpher dioxide in the presence of interfering gases as a function of varying path and corresponding transmittance spectrum for target and interfering gases. (bottom) Percent absorption due to 1 ppb sulpher dioxide and interfering species as a function of varying path and corresponding transmittance spectrum for target and interfering gases.
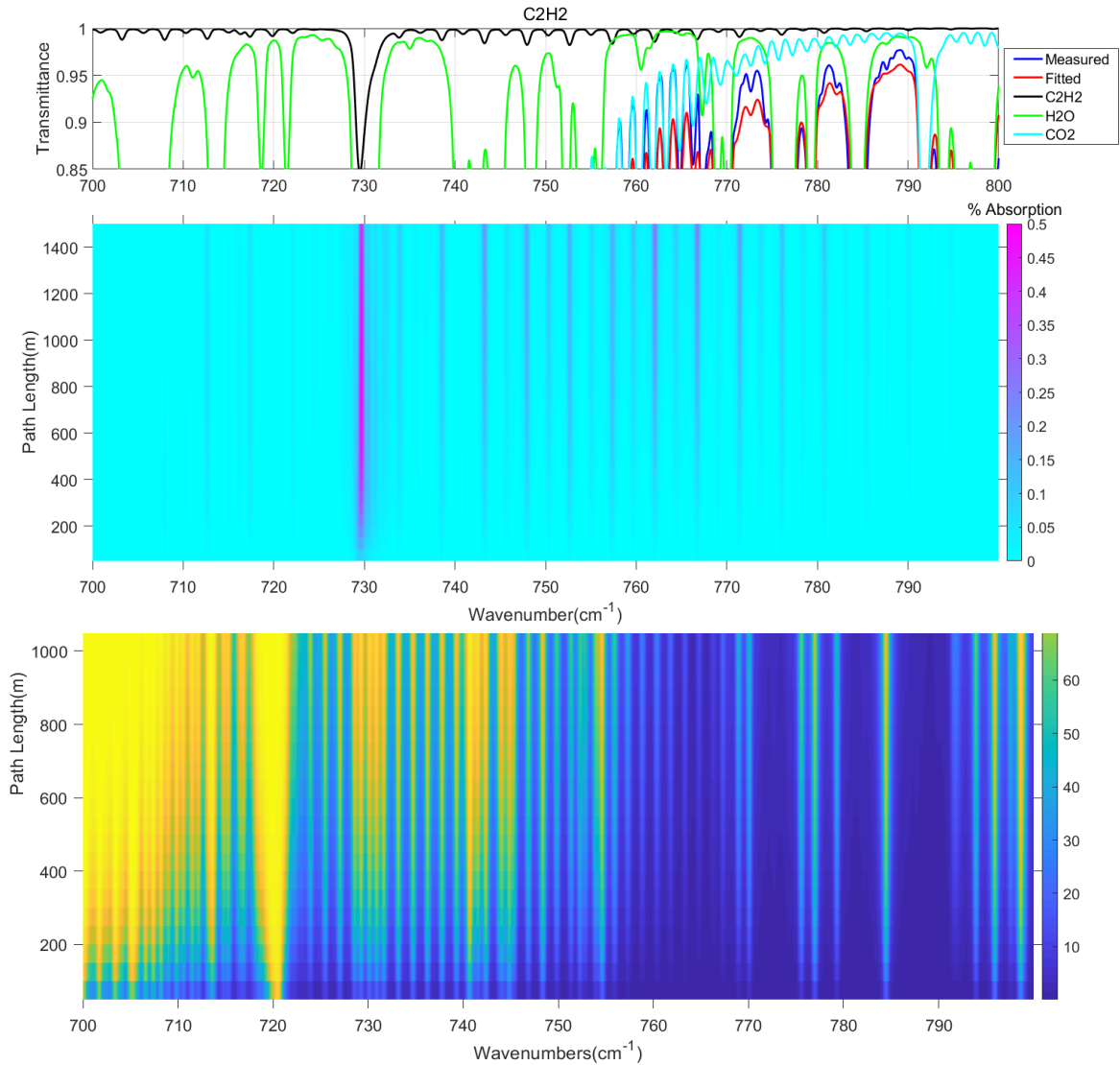
Figure 8: (top) Differential absorption due to 1 ppb acetylene in the presence of interfering gases as a function of varying path and corresponding transmittance spectrum for target and interfering gases. (bottom) Percent absorption due to 1 ppb acetylene and interfering species as a function of varying path and corresponding transmittance spectrum for target and interfering gases.
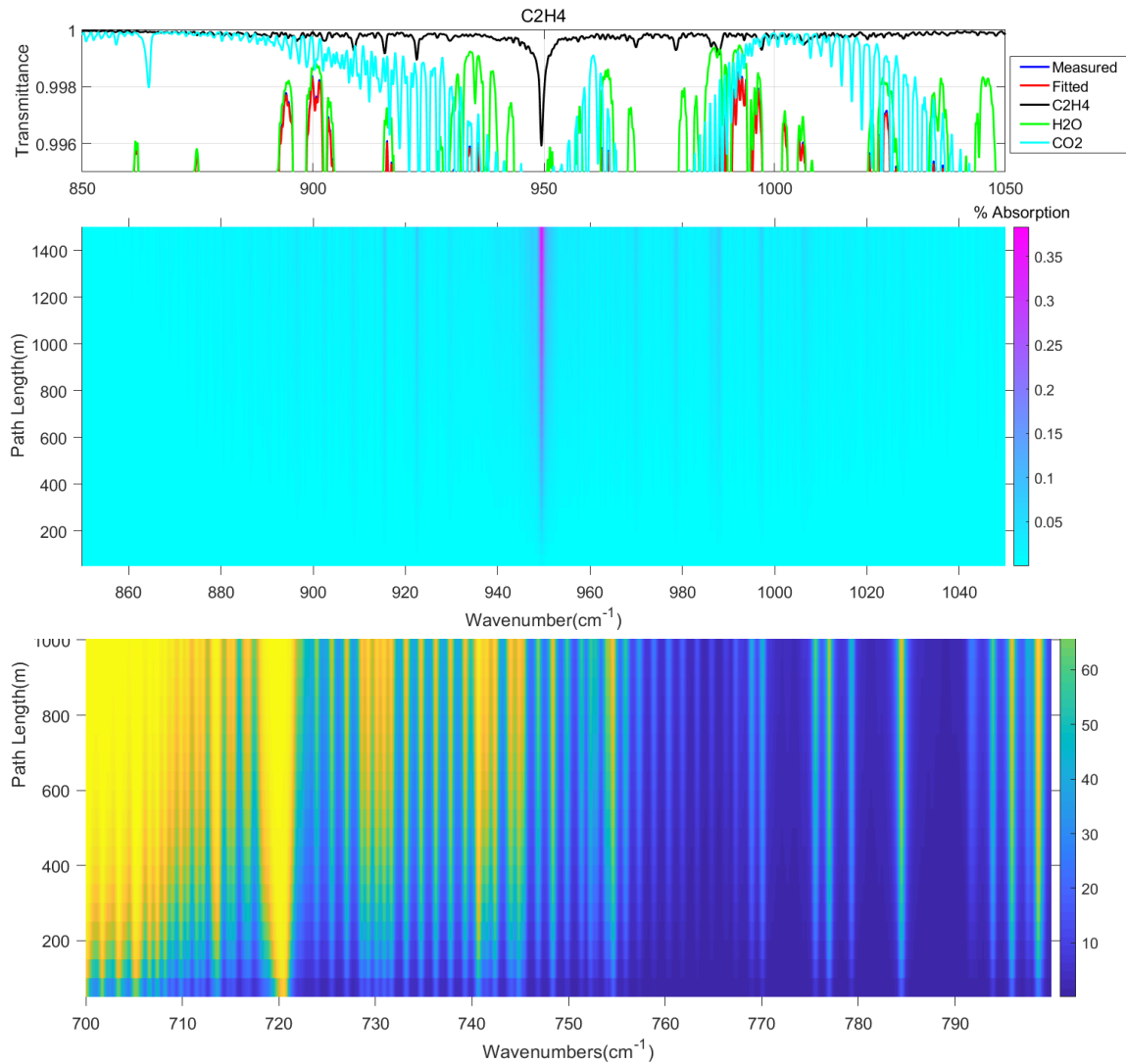
Figure 9: (top) Differential absorption due to 1 ppb ethylene in the presence of interfering gases as a function of varying path and corresponding transmittance spectrum for target and interfering gases. (bottom) Percent absorption due to 1 ppb ethylene and interfering species as a function of varying path and corresponding transmittance spectrum for target and interfering gases.
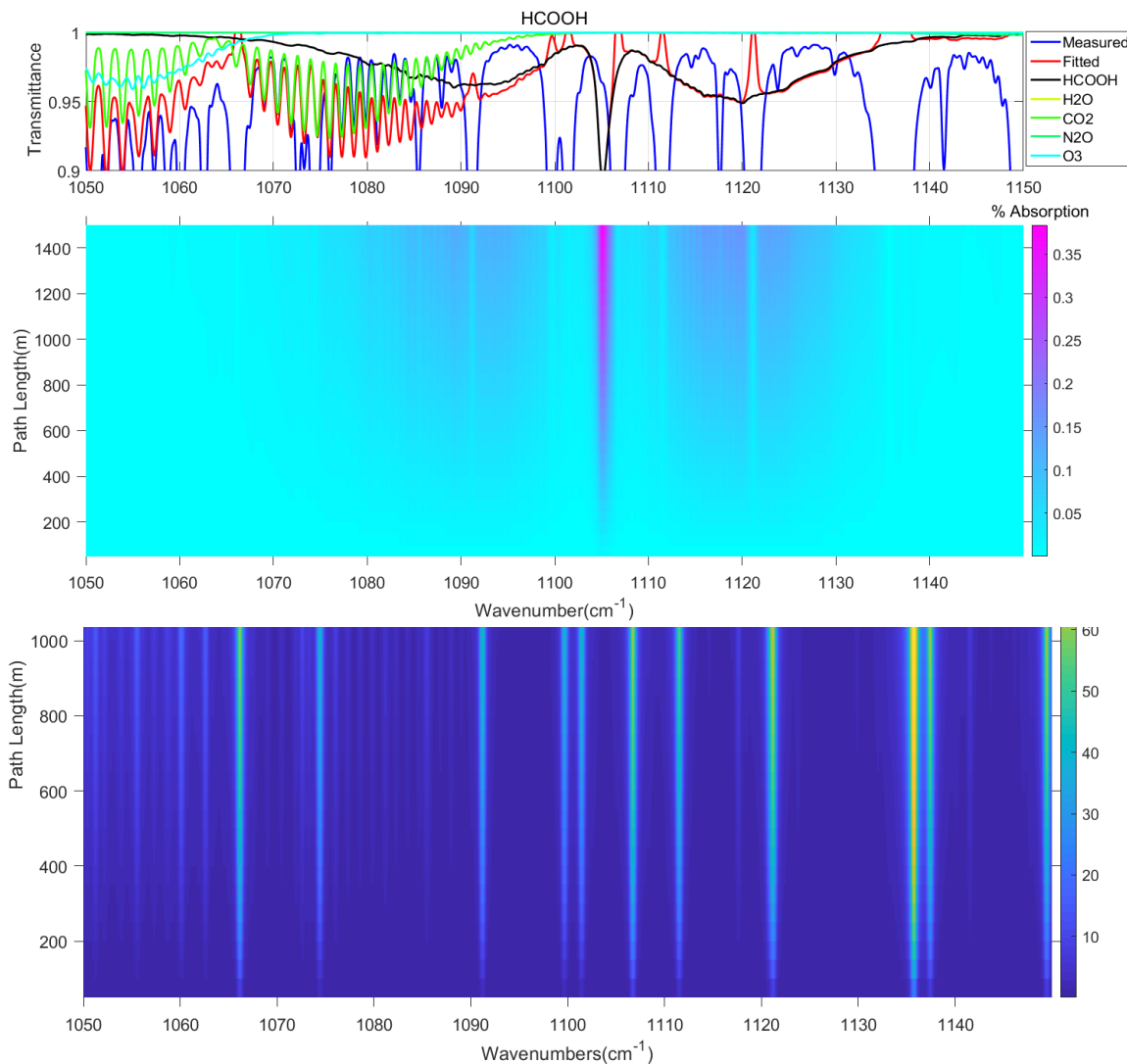
Figure 10: (top) Differential absorption due to 1 ppb formic acid in the presence of interfering gases as a function of varying path and corresponding transmittance spectrum for target and interfering gases. (bottom) Percent absorption due to 1 ppb formic acid and interfering species as a function of varying path and corresponding transmittance spectrum for target and interfering gases.

References

Bacsik, Z., Mink, J. & Keresztury, G. (2004). FTIR Spectroscopy of the Atmosphere. I. Principles and Methods. *Applied Spectroscopy Reviews, 39*(3) 295-363. doi: 10.1081/ASR-200030192

Banwell, C. N., & MacCash, E. M. (1994). Fundamentals of Molecular Spectroscopy (4 ed.). London: McGraw-Hill.

Byrne B. et al. (2020). Monitoring Urban Greenhouse Gases Using Open-Path Fourier Transform Spectroscopy, *Atmosphere-Ocean, 58*(1), 25-45. doi:10.1080/07055900.2019.1698407

Gordon, I., Rothman, L., Hill, C., Kochanov, R., Tan, Y., Bernath, P. & Zak, E. (2017). The HITRAN2016 molecular spectroscopic database. *Journal of Quantitative Spectroscopy and Radiative Transfer, 203*(1) 3-69. doi:10.1016.

Griffith, D. (1996). Synthetic calibration and quantitative analysis of gas-phase FT-IR spectra. *Applied Spectroscopy,* 50(1) 59-70. doi:10.1366/0003702963906627.

Griffith, D. (2002). *FT-IR Measurements of Atmospheric Trace Gases and their Fluxes.* Handbook of Vibrational Spectroscopy. doi:10.1002/0470027320.s6802

Griffith, D., et al. (2017). Long open-path measurements of greenhouse gases in air using near-infrared Fourier transform spectroscopy. *Atmospheric Measurement Techniques, 11*(3) 1549-1563. doi: 10.5194/amt-11-1549-2018

IPCC, 2013: Summary for Policymakers. In: *Climate Change 2013: The Physical Science Basis. Contribution of Working Group I to the Fifth Assessment Report of the Intergovernmental Panel on Climate Change* [Stocker, T.F., D. Qin, G.-K. Plattner, M. Tignor, S.K. Allen, J. Boschung, A. Nauels, Y. Xia, V. Bex and P.M. Midgley (eds.)]. Cambridge University Press, Cambridge, United Kingdom and New York, NY, USA.

Jean M. Bennett and E. J. Ashley. (1965). Infrared Reflectance and Emittance of Silver and Gold Evaporated in Ultrahigh Vacuum. *Applied Optics*, 4(2), 221-224. doi: 10.1364/AO.4.000221

Jarvis. (2003). Open path spectrophotometry (UV, IR, FT-IR).
Instrument engineers' handbook-process measurement and
analysis, volume 1 (4th ed., pp. 1). Instrument Engineers
Handbook: Taylor & Francis.

Smith, T., Wooster, M., Tattaris, M. & Griffith, D. (2011). Absolute
accuracy and sensitivity analysis of OP-FTIR retrievals of CO2,
CH4 and CO over concentrations representative of "clean air"
and "polluted plumes". *Atmospheric Measurement Techniques, 4*(1)
97-116. doi: 10.5194/amt-4-97-2011

Waxman, E. et. al (2017). Intercomparison of open-path trace gas
measurements with two dual-frequency-comb spectrometers.
Atmospheric Measurement Techniques, 10(9), 3295–3311. doi: 10.5194/
amt-10-3295-2017

Wiacek, A., & Strong, K. (2008). Effects of vertical grid discretization in
infrared transmission modeling, Journal of Quantitative
Spectroscopy and Radiative Transfer 109, 2463-2490,
doi:10.1016/j.jqsrt.2008.03.015.

Wiacek, A., Li, L., Tobin, K. & Mitchell, M. (2018a). Characterization

of trace gas emissions at an intermediate port. *Atmospheric*

Chemistry and Physics, 18(19) 13787–13812. doi: 10.5194.

Wiacek, A., et al. (2018b). Open-Path Fourier Transform Infrared (OP-

FTIR) Spectroscopic Measurements of Atmospheric

Composition. *Optical Society of America,* paper FT5B.5.doi: https://

doi.org/10.1364/FTS.2018.FT5B.5